Gut microbiota regulates lacteal integrity by inducing VEGF-C in intestinal villus macrophages

Suh, Sang Heon

2019-04

Suh , S H , Choe , K , Hong , S P , Jeong , S , Mäkinen , T , Kim , K S , Alitalo , K , Surh , C D , Koh , G Y & Song , J-H 2019 , ' Gut microbiota regulates lacteal integrity by inducing VEGF-C in intestinal villus macrophages ' , EMBO Reports , vol. 20 , no. 4 , 46927 . https://doi.org/10.15252/embr.20

http://hdl.handle.net/10138/313016
https://doi.org/10.15252/embr.201846927

acceptedVersion

Article

TRANSPARENT PROCESS

EMBO reports

Gut microbiota regulates lacteal integrity by inducing VEGF-C in intestinal villus macrophages

Sang Heon Suh[1], Kibaek Choe[2], Seon Pyo Hong[3], Seung-hwan Jeong[1], Taija Mäkinen[4], Kwang Soon Kim[5], Kari Alitalo[6], Charles D Surh[5], Gou Young Koh[1,3,*] & Joo-Hye Song[3,**]

Abstract

A lacteal is a blunt-ended, long, tube-like lymphatic vessel located in the center of each intestinal villus that provides a unique route for drainage of absorbed lipids from the small intestine. However, key regulators for maintaining lacteal integrity are poorly understood. Here, we explore whether and how the gut microbiota regulates lacteal integrity. Germ depletion by antibiotic treatment triggers lacteal regression during adulthood and delays lacteal maturation during the postnatal period. In accordance with compromised lipid absorption, the button-like junction between lymphatic endothelial cells, which is ultrastructurally open to permit free entry of dietary lipids into lacteals, is significantly reduced in lacteals of germ-depleted mice. Lacteal defects are also found in germ-free mice, but conventionalization of germ-free mice leads to normalization of lacteals. Mechanistically, VEGF-C secreted from villus macrophages upon MyD88-dependent recognition of microbes and their products is a main factor in lacteal integrity. Collectively, we conclude that the gut microbiota is a crucial regulator for lacteal integrity by endowing its unique microenvironment and regulating villus macrophages in small intestine.

Keywords intestinal lymphatic vasculature; lacteal; macrophage; microbiota; VEGF-C

Subject Categories Immunology; Microbiology, Virology & Host Pathogen Interaction; Vascular Biology & Angiogenesis

DOI 10.15252/embr.201846927 | Received 17 August 2018 | Revised 11 January 2019 | Accepted 21 January 2019

EMBO Reports (2019) e46927

Introduction

A lacteal, the blunt-ended lymphatic capillary at the center of each villus in the small intestine, is a main route for drainage of dietary lipids and lipid-soluble nutrients in the form of lymph, which returns to the systemic circulation via the thoracic duct [1,2]. Lacteals also provide a transport route for immune cells that are distributed in the stromal compartment of the villi, serving an integral part in the gut immune-surveillance system, which is important for promoting tolerance to harmless gut microbiota and food antigens as well as protecting against infection [1–4]. Furthermore, lacteals *per se* serve as the secondary intestinal barrier against pathogen entry with the epithelial cell monolayer of the villi serving as the first barrier [5]. Indeed, dysfunction of intestinal lymphatic vessels in lymphangitis has been raised as a pathogenic factor of inflammatory bowel disease [4,6,7]. Despite the debates on the role of lymphangiogenesis under inflammatory conditions [8], intestinal inflammation was aggravated by blockade of vascular endothelial growth factor receptor 3 (VEGFR3) [9], and was ameliorated by improving lymphatic function by vascular endothelial growth factor C (VEGF-C) stimulation in experimental colitis models [10], emphasizing the protective role of lymphatic vessels for the healthy microenvironment of intestine. Thus, lacteals form an active lymphatic organ with multifaceted functions, rather than being a simple, passive drainage route for lipids.

Emerging evidence indicates that the maintenance of lacteal integrity continuously requires versatile regulatory signals from adjacent stromal cells [2]. The longitudinal smooth muscle cells (SMCs) surrounding lacteals periodically squeeze them via signals from the autonomic nervous system to allow efficient drainage of dietary lipids in villi [11]. In addition, these SMCs produce VEGF-C to maintain lacteal integrity and lipid transport functions mediated through activation of VEGFR3 signaling in the lymphatic endothelial cells (LECs) composing the lacteals [12]. Furthermore, in contrast to the majority of LECs that make up lymphatic vessels in other organs, the LECs of lacteals have low but detectable proliferative capacity under steady-state conditions, driven by continuous activation of Notch ligand delta-like 4 signaling in lacteals [13]. Moreover, adrenomedullin (AM)—calcitonin receptor-like receptor (CLR) signaling plays critical roles in maintaining lacteal morphology and function

1 Graduate School of Medical Science and Engineering, Korea Advanced Institute of Science and Technology (KAIST), Daejeon, Korea
2 Graduate School of Nanoscience and Technology, Korea Advanced Institute of Science and Technology (KAIST), Daejeon, Korea
3 Center for Vascular Research, Institute for Basic Science, Daejeon, Korea
4 Department of Immunology, Genetics and Pathology, Uppsala University, Uppsala, Sweden
5 Academy of Immunology and Microbiology, Institute for Basic Science, Pohang, Korea
6 Translational Cancer Biology Program and Wihuri Research Institute, Biomedicum Helsinki, University of Helsinki, Helsinki, Finland
*Corresponding author. Tel: +82 42 350 5638; E-mail: gykoh@kaist.ac.kr
**Corresponding author. Tel: +82 42 350 5638; E-mail: jhsong0907@gmail.com

[14]. Thus, multiple and dynamic regulators are required to preserve the unique structure and function of lacteals in the small intestine.

Small intestinal villi are covered with many kinds of commensal microbes that have co-evolved with the host mutualistically [15,16]. To protect the intestine against enteric pathogen infection, the gut microbiota produces a short-chain fatty acid that enhances intestinal epithelial cell barrier function and promotes secretion of mucus and antimicrobial peptides, limiting pathogen colonization [17]. In addition, microbiota and associated metabolites regulate the development and homeostasis of gut immune systems [18–22]. Growing evidence indicates that the microbiota is responsible not only for local tissue homeostasis but also for homeostasis, such as metabolism and energy balance, in distant organs [23,24]. Gut microbiota even influence brain function, behavior, and mental health [25–28]. The postnatal development of intestinal vasculature is driven by gut microbiota [29], where tissue factor and protease-activated receptor promote vascular remodeling [30]. While the diverse organ-specific roles of gut microbiota have been extensively studied, their role in lacteals is so far only limitedly understood [31].

In the present study, we explored whether and how the gut microbiota regulates lacteal integrity. Intriguingly, we found lacteal regression in germ-depleted adult mice. We unveiled that VEGF-C derived from macrophages in the intestinal villi is a key factor in gut microbiota-mediated maintenance of lacteal integrity.

Results

Gut microbiota is crucial to maintain lacteal structure

To investigate the role of gut microbiota in maintaining lacteal integrity, we depleted the microbiota by administration of an antibiotic cocktail (ABX) to 8-week-old mice for 4 weeks (Fig 1A). Depletion was confirmed with no detectable bacterial colony in the feces of the mice at the end of the ABX treatment (Fig 1B). Body weight was not different between vehicle- and ABX-treated mice (Appendix Fig S1). Using whole-mount immunostaining of the small intestine, we visualized the epithelial lining, capillary plexus, and lacteal in villi of the duodenum, jejunum, and ileum (Fig 1C). Among these, the most striking finding was reduced lacteal length by ABX treatment (Fig 1D). Quantitative analyses revealed that absolute and relative lacteal lengths reduced by 15–17% in jejunum and ileum, but no change was detected in duodenum of ABX-treated mice compared to vehicle-treated mice, while the villus lengths were not different between the two groups along the entire length of intestine (Fig 1E). We attributed this differential effect to the differential burden of gut microbiota in different parts of the intestine, i.e., much more microbiota in jejunum and ileum than in duodenum [15]. The number of Prox1$^+$ LECs and VEGFR3 expression decreased by 31 and 65%, respectively, in the jejunum lacteals of ABX-treated mice compared to vehicle-treated animals (Fig 1F and G). However, compared to vehicle-treated mice, the overall villus structure, capillary plexus length, and capillary vascular endothelial growth factor receptor 2 (VEGFR2) expression were not apparently altered in ABX-treated mice; even so, the capillary plexus network in the villi of ABX-treated mice was substantially less complex (Figs 1D and EV1A), as has been previously reported [29].

We examined whether the ABX treatment affects survival of LECs in lacteals by immunostaining for caspase-3. No difference in the number of lacteals with caspase-3$^+$ LECs was found between vehicle- and ABX-treated mice (Appendix Fig S2A). Furthermore, to test whether ABX *per se* has any direct toxic effect on the lacteals, primary cultured human dermal LECs (HDLECs) were exposed to ABX at a concentration comparable to the *in vivo* experiments for up to 48 h (Appendix Fig S2B). However, no obvious changes in Prox1 expression and number of apoptotic cells induced by the ABX exposure were detected in the cultured HDLECs, implying that ABX *per se* do not exert a direct adverse effect on the LECs of lacteals.

To examine whether depletion of gut microbiota causes regression of lymphatic vessels in other organs, we compared lymphatic vessels of ear skin, trachea, diaphragm, and inguinal lymph nodes between vehicle-treated and ABX-treated mice but observed no apparent differences (Appendix Fig S3). Overall, depletion of gut microbiota resulted in lacteal regression specifically in the villi of the jejunum and ileum of adult mice.

Gut microbiota determines proper lacteal function for dietary lipid drainage

To determine whether germ depletion influences unique junctional structure that is closely related to function in lacteals [32], we compared VE-cadherin$^+$ LEC junctional patterns between vehicle- and ABX-treated mice. Similar to LEC junctional organization of lymphatic capillaries in other organs [32] (Fig EV1B), discontinuously sealed button-like LEC junctions (52%) predominated in lacteals, but continuously sealed zipper-like (33%) and mixed patterns (15%) were also observed (Fig 2A and B), while blood endothelial cell junctions of the capillary plexus were entirely continuously sealed (Fig EV1C). Depletion of gut microbiota reduced the proportion of button-like junctions by 29% but increased the proportion of zipper-like junctions by 26% in lacteals (Fig 2A and B).

To evaluate the effect of gut microbiota on lacteal function, we measured lipid clearance from the lamina propria of villi after intraluminal loading of boron-dipyrromethene fluorescent-conjugated fatty acid (BODIPY-FA) using an intravital imaging system (Fig 2C and D). Although the fluorescence signal intensity of BODIPY-FA increased more rapidly in the lamina propria of villi of ABX-treated mice, presumably because of mucosal layer thinning secondary to germ depletion, the peak levels at around 16 min were not significantly different between vehicle- and ABX-treated mice. Of note, absolute and normalized residual signal of BODIPY-FA in the lamina propria compartment at 36 min after loading was significantly higher in ABX-treated compared to vehicle-treated mice (Fig 2C and D), implying that drainage of dietary lipids is functionally compromised in ABX-induced germ-depleted animals. Transmission electron microscopy examination of lacteals (Fig 2E and F) revealed that chylomicrons pass through open junctions between LECs and enter the lacteal lumen in vehicle-treated mice. Together with the observation of vesicles containing lipoprotein particles and large caveolae, these suggested both paracellular (lipid absorption via open junctions between LECs) and transcellular (cellular uptake of lipid and excretion into the lacteal lumen) mechanisms of lipid transport. In contrast, the junction in ABX-treated mice was sparsely open, and virtually none of chylomicron particles were able to move through LEC junctions. We further

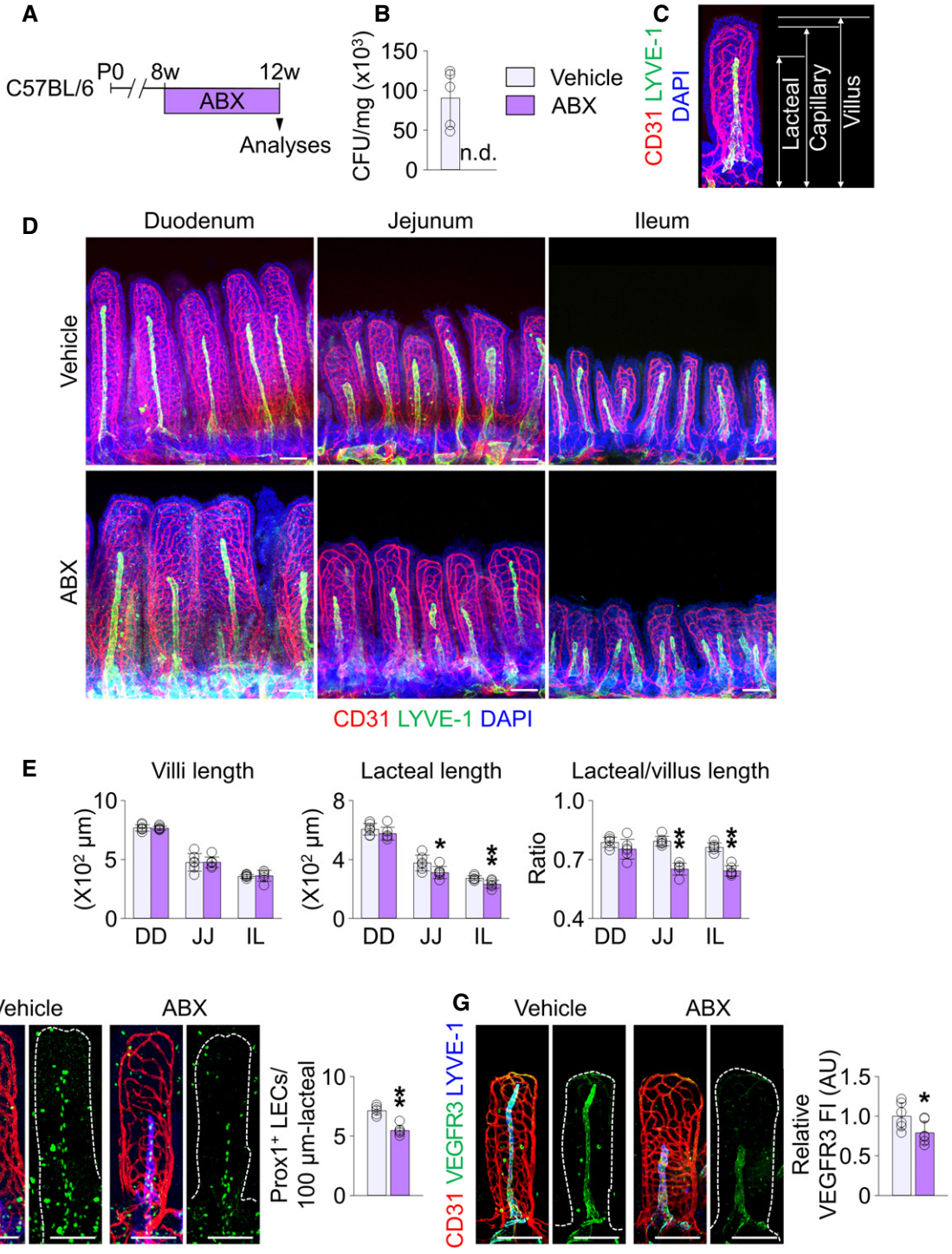

Figure 1. Depletion of gut microbiota causes morphological defects in lacteals.

A Diagram for depletion of gut microbiota in C57BL/6 adult mice by administration of ABX starting at 8 weeks for 4 weeks and their analyses at 12 weeks.

B Comparison of bacterial colony-forming unit (CFU) in feces from vehicle- and ABX-treated mice (n = 5 mice/group). n.d., non-detectable.

C Representative image and measurements of lengths for CD31$^+$/LYVE-1$^+$ lacteal, CD31$^+$/LYVE-1$^-$ capillary plexus, and DAPI$^+$ villus.

D, E Images and comparisons of villi lengths and absolute and relative lacteal lengths in duodenum (DD), jejunum (JJ) and ileum (IL) of vehicle- or ABX-treated mice. Each dot indicates mean value of 5–10 villi in a mouse (n = 6 mice/group).

F, G Images and comparisons of the number of Prox1$^+$ LECs within initial 100 μm portion (F) and VEGFR3 expression (G), presented as relative fluorescence intensity (FI) in CD31$^+$/LYVE-1$^+$ lacteals of jejunum from vehicle- or ABX-treated mice. Dotted lines outline villi. Each dot indicates mean value of 5–10 villi in a mouse (n = 6 mice/group). AU, arbitrary unit.

Data information: All scale bars, 100 μm. Data are represented as means ± SD. *P < 0.05; **P < 0.01 versus vehicle-treated mice by two-tailed unpaired Student's t-test.

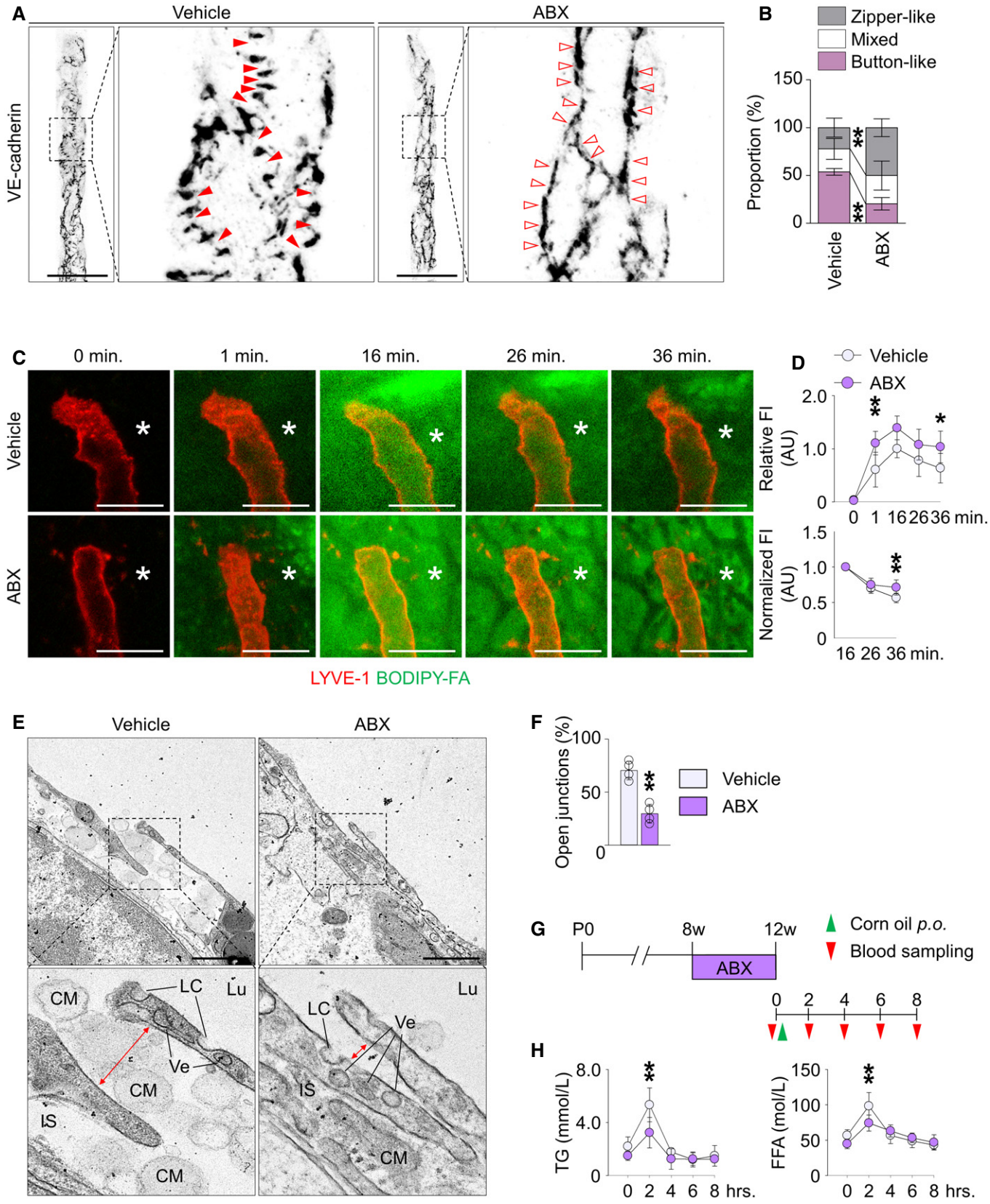

Figure 2.

Figure 2. Depletion of gut microbiota alters LEC junctions in lacteals and impedes dietary lipid absorption to systemic circulation.

A, B Images and comparison of VE-cadherin LEC junctions in lacteals of jejunum between vehicle- and ABX-treated mice. Each boxed portion is highly magnified for visualization of detailed distributions of VE-cadherin to distinguish button-like (red arrowheads), zipper-like (open arrowheads), and mixed LEC junctions in lacteals (n = 6 mice/group, 5–10 villi/mouse). Scale bars, 50 μm.

C, D Representative intravital imaging and quantification of lipid clearance from lamina propria via lacteals. Asterisks indicate the site in lamina propria where fluorescence intensity (FI) was measured. Relative FI divided by mean FI of controls at 16 min (left) and normalized FI divided by FI at 16 min in each villus (right) after initial loading of BODIPY-FA were quantified. For normalization of FI, villi that showed peak intensity earlier or later than 16 min were excluded (n = 5–7 mice/group, 5–10 villi/mouse). Scale bars, 100 μm.

E, F Representative images from transmission electron microscopic examination of lacteals and quantification of frequency of open junctions (n = 4 mice/group, 4–6 images/mouse). Jejunum of vehicle- and ABX-treated mice were harvested 2 h after oral lipid loading. Note that the junction between LECs (red colored bidirectional arrows) is open in vehicle-treated mice, but not in ABX-treated mice. CM, chylomicron; IS, interstitium of lamina propria; LC, large caveola; Lu, lacteal lumen; Ve, vesicle containing lipoproteins. Scale bars, 1 μm.

G Diagram for ABX treatment and sampling of systemic blood at indicated time points after oral loading of corn oil into C57BL/6 adult mice.

H Comparisons of serum triglyceride (TG) and free fatty acids (FFA) at indicated time points in vehicle- and ABX- treated mice (n = 5–7 mice/group).

Data information: Data are represented as means ± SD. *P < 0.05; **P < 0.01 versus vehicle-treated mice by two-way ANOVA with Bonferroni *post hoc* analysis.

assessed lacteal function by measuring triglyceride (TG) and free fatty acid (FFA) levels in the systemic circulation at different time points after oral administration of corn oil to the animals (Fig 2G). Compared to vehicle-treated mice, ABX-treated mice had 39 and 24% reduction in peak TG and FFA levels at 2 h after the corn oil administration, respectively (Fig 2H). Collectively, these results indicate that the intestinal microbiota plays crucial roles in maintaining the structural and functional integrity of lacteals.

Microbial colonization facilitates lacteal maturation during the postnatal weaning period

Lacteals begin to develop during the embryonic period but continue to grow during the postnatal period [33]. Microbial composition also continuously evolves after birth until weaning from lactation around postnatal day 21 (P21) in mice [34], as we confirmed the quantitative expansion of microbiota between P10 and P28 (Appendix Fig S4). To investigate whether postnatal microbial expansion controls lacteal maturation, we analyzed and compared intestinal villi of pups from vehicle- and ABX-treated groups at P7, P14, and P28. During the milk-feeding period (P7–P14), we found no distinct differences in lacteal lengths between vehicle- and ABX-treated animals (Fig 3A and B). However, at P28, absolute and relative lacteal lengths decreased by 16–23% in the jejunum of ABX-treated mice (Fig 3A and B). ABX treatment also reduced the number of $Prox1^+$ LECs in lacteals by 40% compared to the vehicle-administered group (Fig 3C and D). Of note, 66–73% of LEC junctions in lacteals were zipper-like at P7, and the proportion gradually decreased at P14 and P28; a button-like LEC junction was rarely found at P7 but emerged at P14, and the proportion increased up to 47% at P28 (Fig 3E and F). No noticeable differences were found in LEC junctions between vehicle- and ABX-treated mice at P7 and P14 (Fig 3E and F); at P28, though, the proportion of button-like junctions was 26% less, while that of zipper-like LEC junctions was 29% more in ABX-treated mice compared to vehicle-treated animals (Fig 3E and F). These data collectively indicate that lacteals continue to mature in length and junctional pattern postnatally, and that expansion of the gut microbiota between P14 and P28 promotes these processes in the villi.

Microbiota colonization restores lacteal defects in germ-free mice

To confirm further the role of gut microbiota in the lacteal integrity, we examined lacteals in germ-free (GF) mice [22]. GF mice harbored morphological defects in lacteals similar to those of ABX-treated animals (Fig 4). Compared to mice bred in specific pathogen-free (SPF) conditions [SPF mice], absolute and relative lacteal lengths decreased by 20–24% in jejunum and ileum but did not change in duodenum, while the villus length increased by 5–7% (Fig 4A and B), as previously reported [35]. The $Prox1^+$ LEC number, VEGFR3 expression levels, and proportion of button-like junctions decreased by 20, 88, and 77%, respectively, in jejunum lacteals of GF mice (Fig 4C–F). Compared to SPF mice, TG level in the lymph of thoracic duct was reduced in GF mice, indicating the compromise in the lipid drainage function of lacteals (Appendix Fig S5).

To explore whether the lacteal defects in GF mice are reversible, we conventionalized the GF animals [CONV mice]. CONV mice showed normalized lacteal lengths, Prox1 and VEGFR3 expression, and LEC junctional patterns, all comparable to those of SPF mice (Fig 4). Nevertheless, we detected no changes in lymphatic vessels of other major organs such as ear skin, tracheal mucosa, diaphragm, and lymph node of GF mice (Fig EV2). These findings imply that lacteals have a relatively wide range of plasticity to gut microbiota for maintaining their integrity.

Villus macrophages respond to microbial stimuli to produce VEGF-C

To uncover how gut microbiota regulates lacteal integrity, we first assessed attenuated VEGFR3 expression in the lacteals of both ABX-treated and GF mice. To clarify whether downregulation of VEGFR3 affects lacteal integrity, we conditionally deleted VEGFR3 in lacteals using $VEGFR3^{i\Delta LEC}$ mice, which were generated by crossing the $VEGFR3^{fl/fl}$ mice [36] with the Prox1-$CreER^{T2}$ animals [37]. Efficient VEGFR3 deletion was observed in the lacteals of $VEGFR3^{i\Delta LEC}$ mice at 4 weeks after tamoxifen injection (Fig 5A and B). Compared to wild-type (WT) mice, the absolute and relative lacteal lengths decreased by 13–17%, 17–19%, and 23–25% in duodenum, jejunum, and ileum, respectively, of the $VEGFR3^{i\Delta LEC}$ mice (Fig 5C and D), as previously reported [12]. Moreover, the number of $Prox1^+$ LECs also fell by 38% (Fig 5E and F). Strikingly, button-like LEC junctions almost completely (94%) disappeared in the lacteals of $VEGFR3^{i\Delta LEC}$ mice (Fig 5G and H). Accordingly, compared to WT mice, $VEGFR3^{i\Delta LEC}$ mice showed defected dietary lipid absorption (Fig 5I).

Based on the similar phenotypes in lacteals between GF mice and $VEGFR3^{i\Delta LEC}$ mice, we hypothesized that VEGF-C, a ligand

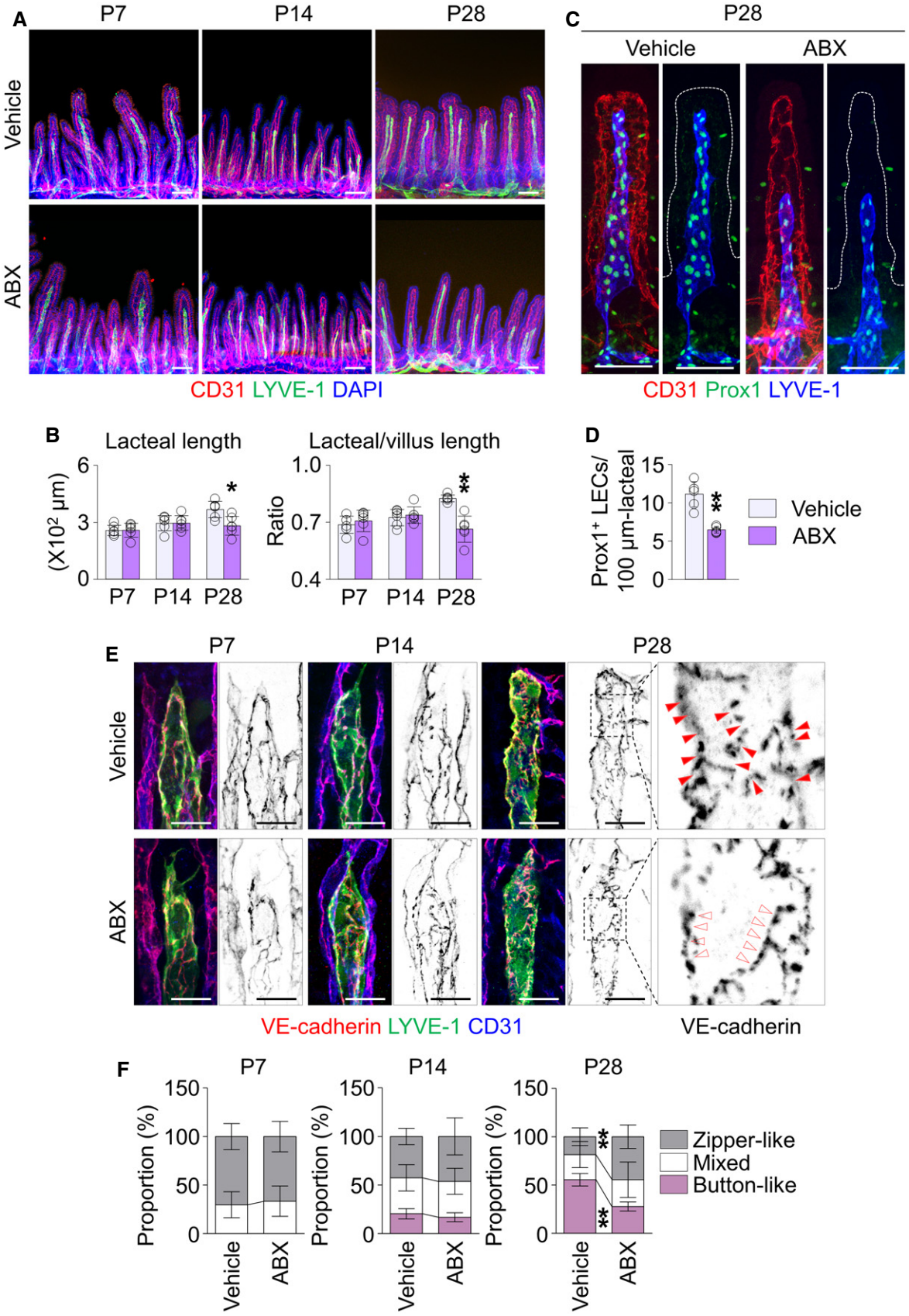

Figure 3.

Figure 3. Depletion of gut microbiota delays lacteal maturation during postnatal period.

A, B Images and comparisons of absolute and relative lacteal lengths in jejunum between vehicle- or ABX-treated mice at P7, P14, and P28. Each dot indicates mean value of 5–10 villi in a mouse (n = 6 mice/group). Scale bars, 100 μm.

C, D Images and comparisons of number of Prox1$^+$ LECs within initial 100 μm portion in CD31$^+$/LYVE-1$^+$ lacteals of jejunum from vehicle- or ABX-treated mice. Dotted lines outline villi. Each dot indicates mean value of 5–10 villi in a mouse (n = 6 mice/group). Scale bars, 100 μm.

E, F Images and comparisons of proportions of each VE-cadherin LEC junctions in CD31$^+$/LYVE-1$^+$ lacteals in jejunum between vehicle- or ABX-treated mice at P7, P14, and P28. Button-like (red arrowheads) and zipper-like (open arrowheads) junctions are indicated in each magnified box in right (n = 6 mice/group, 5–10 villi/mouse). Scale bars, 25 μm.

Data information: Data are represented as means ± SD. *P < 0.05; **P < 0.01 versus vehicle-treated mice by two-tailed unpaired Student's t-test (B, D) and by two-way ANOVA with Bonferroni *post hoc* analysis (F).

for VEGFR3, might be low in gut microbiota-depleted or GF conditions. Indeed, VEGF-C protein level in the tissue lysates of jejunum and ileum was 35% less in ABX-treated mice compared to vehicle-treated animals, whereas vascular endothelial growth factor (VEGF-A) protein level did not differ between the two groups (Appendix Fig S6A). The reduction of tissue VEGF-C protein level was also observed in GF mice, compared to SPF mice (Fig 5J). Conventionalization of GF mice increased both VEGF-C mRNA and protein levels in the tissue lysates, which is equivalent to the level of SPF mice (Fig 5J and K). Although angiopoietin 1 [38], angiopoietin 2 [39], transforming growth factor β1 [40], collagen- and calcium-binding EGF domains 1 [41], and a disintegrin and metalloproteinase with thrombospondin motifs 3 [42] have been known to regulate lymphangiogenesis and lymphatic remodeling, tissue mRNA levels between vehicle- and ABX-treated groups were not different (Appendix Fig S6B). The mRNA level of delta-like 4, which is also known to organ-specifically regulate the lacteal maintenance [13], did not significantly differ in the intestinal LECs between the two groups (Appendix Fig S6C).

Next, to seek which cells produce VEGF-C in response to gut microbial recognition, we considered the SMCs surrounding lacteals and macrophages in the lamina propria compartment (defined as "villus macrophages") as strong candidates, which are already known as sources of VEGF-C in the intestine [12,43,44]. The VEGF-C expression level of CD45$^-$ stromal cells, including SMCs, and CD45$^+$ MHCII$^+$ F4/80$^+$ villus macrophages, was comparable in vehicle-treated mice (Fig 6A). However, while no significant difference was found in the villi CD45$^-$ stromal cells between the vehicle and ABX groups, the villus macrophages of ABX-treated mice showed a reduction in VEGF-C expression by 46% (Fig 6B). Moreover, immunostaining revealed that alignment and density of the SMCs along the entire length of the small intestine were not affected by germ depletion by ABX treatment, GF condition or conventionalization (Fig EV3). In contrast, the number of villi F4/80$^+$ macrophages decreased by 45 and 95% in jejunum and ileum, respectively, but not in the duodenum of ABX-treated mice (Fig 6C and D). Flow cytometric analysis revealed that the number of MHCII$^+$ F4/80$^+$ villus macrophages isolated from jejunum and ileum decreased by 49% in ABX-treated mice (Fig 6E). Further characterization of the macrophage phenotypes revealed that MHCII$^+$ F4/80$^+$ villus macrophages also express CX3CR1. MHCII$^+$ F4/80$^+$ CX3CR1$^+$ villus macrophages isolated from jejunum and ileum decreased by 41% in ABX-treated mice (Fig 6F). These findings indicate that the gut microbiota controls the number of villus macrophages and their VEGF-C production in jejunum and ileum.

Villus macrophages are indispensable for lacteal integrity

To define the role of villus macrophages in lacteal integrity, we depleted the CX3CR1$^+$ villus macrophages by using CX3CR1-DTR mice [45]. With intraperitoneal administration of diphtheria toxin (DT) for 2 weeks (Fig 7A), CD45$^+$ MHCII$^+$ F4/80$^+$ villus macrophages were depleted up to 80% in the jejunum and ileum of CX3CR1-DTR mice (Fig 7B and C). Accordingly, VEGF-C mRNA level in the whole tissue lysate of jejunum and ileum was decreased by 57% in CX3CR1-DTR mice compared with the WT mice (Fig 7D). Intraperitoneal administration vehicle or DT in WT did not affect the tissue VEGF-C mRNA level (Appendix Fig S7). Compared to WT, the absolute and relative lacteal lengths decreased by 11–27% in the jejunum and ileum of CX3CR1-DTR animals (Fig 7E and F), and Prox1$^+$ LEC number and VEGFR3 expression decreased by 20 and 24%, respectively, in the lacteals of CX3CR1-DTR mice (Fig 7G and H). Finally, the proportion of button-like junctions fell by 70% in lacteals of CX3CR1-DTR mice compared to WT animals (Fig 7I and J). Thus, these data indicate the indispensable role of villus macrophages for lacteal integrity.

MyD88-dependent signal regulates VEGF-C production in macrophages to maintain lacteal integrity

Macrophages express TLRs 1–9 to sense microbes and microbial products [37], except for TLR3, the downstream signals of which are in large transduced by their adaptor molecule, myeloid differentiation primary-response protein 88 (MyD88) [46]. To define whether the microbe recognition is a direct stimulation for VEGF-C production in villus macrophages, we conditionally deleted MyD88 in these cells using MyD88$^{\Delta MP}$ mice, which were generated by crossing MyD88$^{flox/flox}$ mice [47] with LysM-Cre animals [48] (Fig 8A). Compared to WT mice, the number of CD45$^+$ MHCII$^+$ F4/80$^+$ macrophages and VEGF-C mRNA transcription levels in sorted villus macrophages (Fig 8B–D) was reduced respectively by 30 and 52% in the jejunum and ileum of MyD88$^{\Delta MP}$ mice. Of note, absolute and relative lacteal lengths decreased by 15–20% in MyD88$^{\Delta MP}$ mice (Fig 8E and F). Moreover, Prox1$^+$ LEC number and VEGFR3 expression decreased respectively by 18 and 23% in the jejunum of MyD88$^{\Delta MP}$ mice (Fig 8G and H). Finally, the proportion of button-like junctions was 53% less in the lacteals of MyD88$^{\Delta MP}$ mouse jejunum (Fig 8I and J). These findings indicate that MyD88-dependent recognition of microbes or microbial product is a direct stimulation for VEGF-C expression in villus macrophages to maintain lacteal integrity.

We next determined which subtype of TLRs is specifically involved in VEGF-C production of villus macrophages. Sorted villus

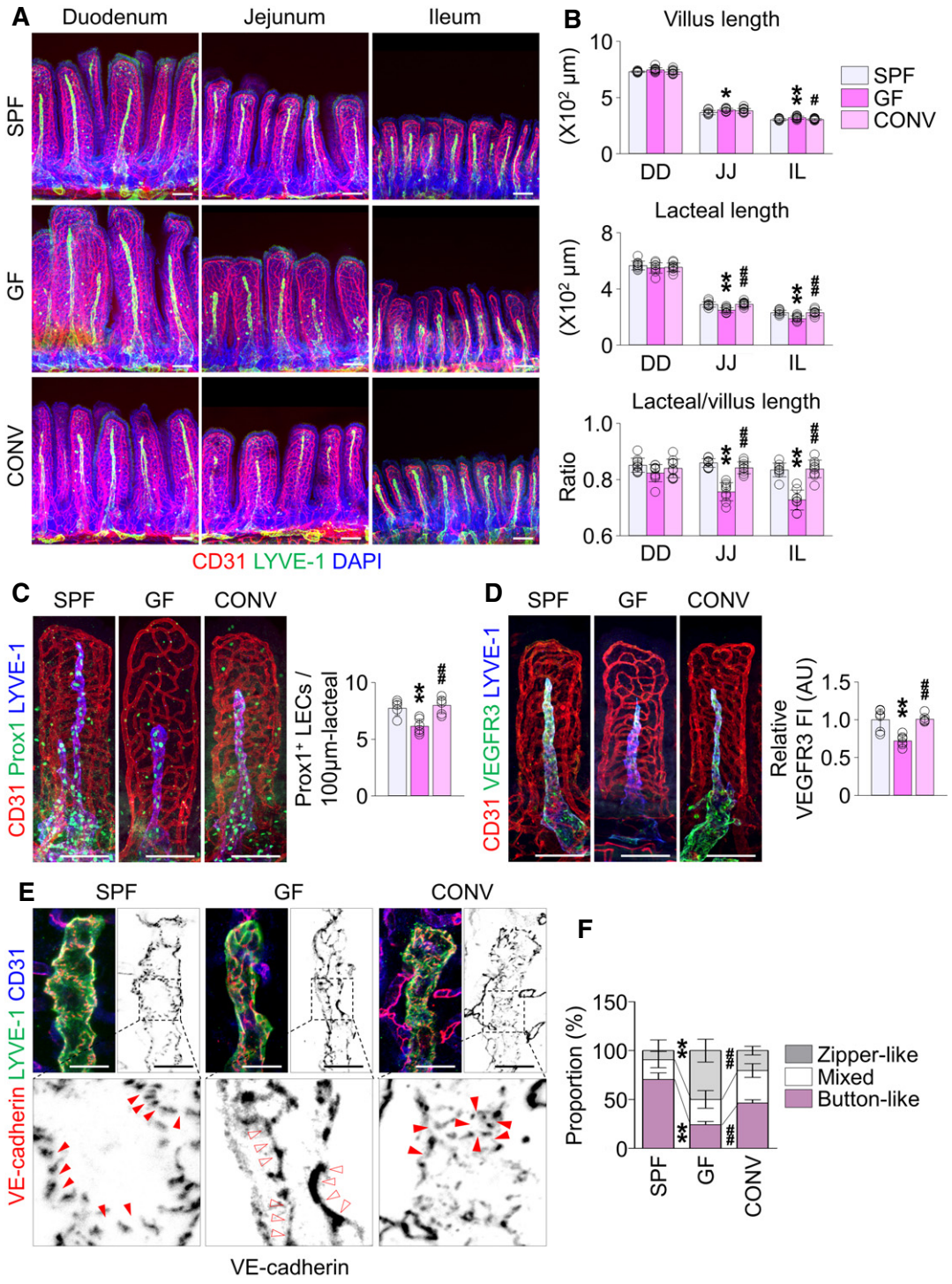

Figure 4. Microbiota colonization restores lacteal defect in GF mice.

A, B Images and comparisons of absolute and relative lacteal lengths in duodenum (DD), jejunum (JJ), and ileum (IL) of 8-week-old SPF, GF or CONV mice. Each dot indicates mean value of 5–10 villi in a mouse (n = 9 mice/group). Scale bars, 100 μm.

C, D Images and comparisons of the number of Prox1$^+$ LECs within initial 100 μm portion (C) and VEGFR3 expression (D, presented as relative fluorescent intensity (FI)) in CD31$^+$/LYVE-1$^+$ lacteals of jejunum from SPF, GF, and CONV mice. Each dot indicates mean value of 5–10 villi in a mouse (n = 6 mice/group). AU, arbitrary unit. Scale bars, 100 μm.

E, F Images and comparison of proportions of each VE-cadherin LEC junctions in CD31$^+$/LYVE-1$^+$ lacteals in jejunum among SPF, GF, and CONV mice. Button-like (red arrowheads) and zipper-like (open arrowheads) junctions are indicated in each magnified box in below (n = 6 mice/group, 5–10 villi/mouse). Scale bars, 25 μm.

Data information: Data are represented as means ± SD. $^{**}P < 0.01$ versus SPF mice; $^{\#\#}P < 0.01$ versus GF mice by one-way ANOVA with Tukey's multiple comparison test (B-D) and by two-way ANOVA with Bonferroni *post hoc* analysis (F).

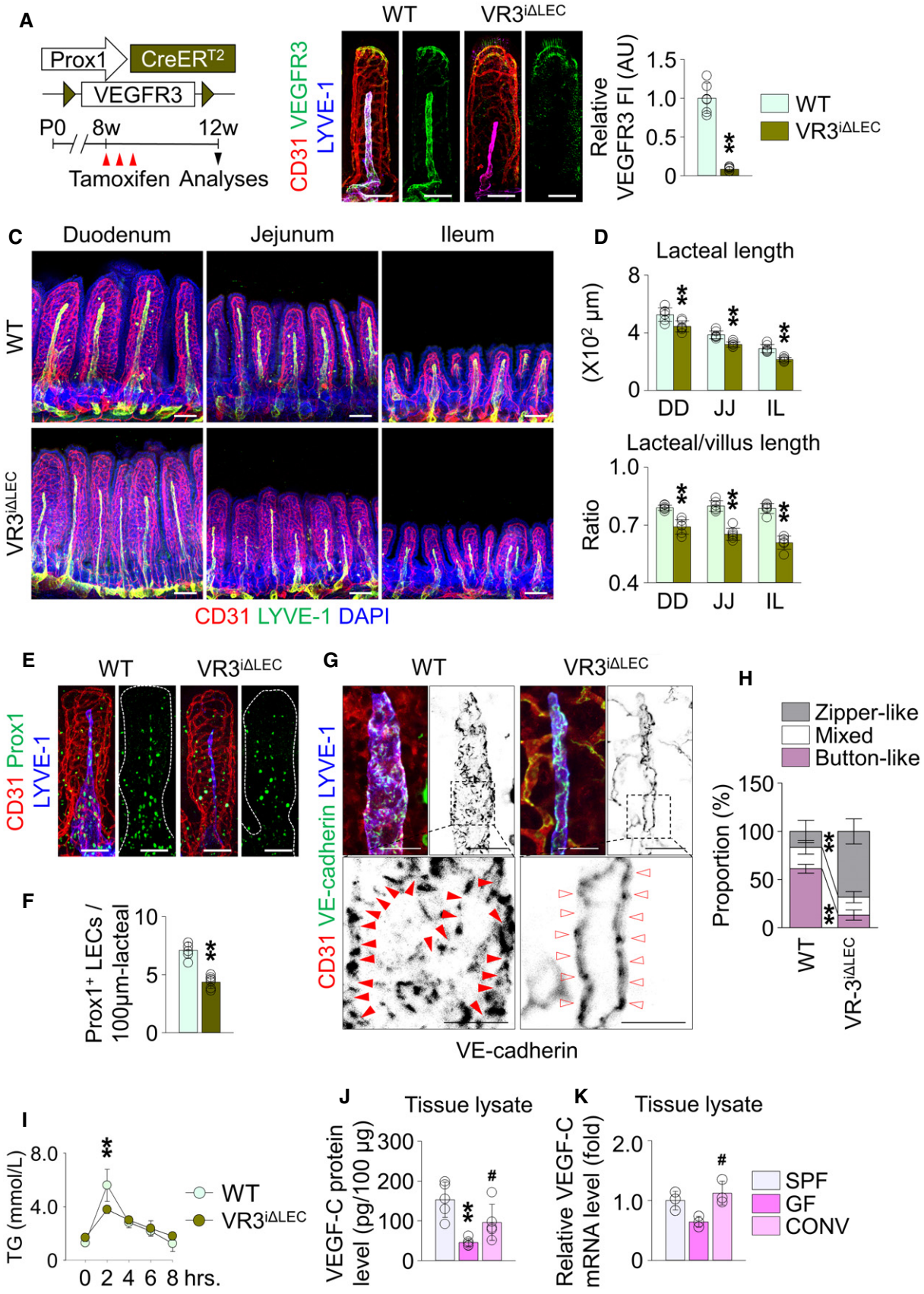
A
Prox1
CreER^{T2}
VEGFR3
P0
8w
12w
Tamoxifen
Analyses
WT
VR3^{iΔLEC}
CD31 VEGFR3 LYVE-1
Relative VEGFR3 FI (AU)
1.5
1.0
0.5
0
**
WT
VR3^{iΔLEC}
C
Duodenum
Jejunum
Ileum
WT
VR3^{iΔLEC}
CD31 LYVE-1 DAPI
D
Lacteal length
(X10^2 μm)
8
4
0
**
DD
JJ
IL
Lacteal/villus length
Ratio
1.0
0.7
0.4
E
WT
VR3^{iΔLEC}
CD31 Prox1 LYVE-1
F
Prox1$^+$ LECs / 100μm-lacteal
10
5
0
G
WT
VR3^{iΔLEC}
CD31 VE-cadherin LYVE-1
VE-cadherin
H
Zipper-like
Mixed
Button-like
Proportion (%)
150
100
50
0
WT
VR-3^{iΔLEC}
I
TG (mmol/L)
8.0
4.0
0
0 2 4 6 8 hrs.
WT
VR3^{iΔLEC}
J
Tissue lysate
VEGF-C protein level (pg/100 μg)
300
200
100
0
#
K
Tissue lysate
Relative VEGF-C mRNA level (fold)
2.0
1.0
0
#
SPF
GF
CONV

Figure 5.

Figure 5. Depletion of gut microbiota reduces the expression of VEGF-C, which is essential for lacteal maintenance in intestinal villi.

A Diagram for LEC-specific ablation of VEGFR3 in adult mice ($VR3^{i\Delta LEC}$).

B Images and comparison of VEGFR3 expression [presented as relative fluorescent intensity (FI)] in $CD31^+/LYVE\text{-}1^+$ lacteals of jejunum between WT and $VR3^{i\Delta LEC}$ mice. Each dot indicates mean value of 5–10 villi in a mouse (n = 6 mice/group). AU, arbitrary unit. Scale bars, 100 μm.

C, D Images and comparisons of absolute and relative lacteal lengths in duodenum (DD), jejunum (JJ), and ileum (IL) of WT and $VR3^{i\Delta LEC}$ mice. Note that, in addition to the alterations in the lacteal lengths in $VR3^{i\Delta LEC}$ mice, diameters of the lacteal also shrank by VEGFR3 ablation. Each dot indicates mean value of 5–10 villi in a mouse (n = 6 mice/group). Scale bars, 100 μm.

E, F Images and comparisons of number of $Prox1^+$ LECs within initial 100 μm portion in $CD31^+/LYVE\text{-}1^+$ lacteals of jejunum from WT and $VR3^{i\Delta LEC}$ mice. Dotted lines outline villi. Each dot indicates mean value of 5–10 villi in a mouse (n = 6 mice/group). Scale bars, 100 μm.

G, H Images and comparison of proportions of each VE-cadherin LEC junctions in $CD31^+/LYVE\text{-}1^+$ lacteals in jejunum from WT and $VR3^{i\Delta LEC}$ mice. Button-like (red arrowheads) and zipper-like (open arrowheads) junctions are indicated in each magnified box in below (n = 6 mice/group, 5–10 villi/mouse). Scale bars, 25 μm.

I Comparisons of serum triglyceride (TG) at indicated time points in WT and $VR3^{i\Delta LEC}$ mice (n = 6 mice/group).

J, K Comparison of protein (J) and mRNA (K) levels of VEGF-C in the whole tissue of jejunum and ileum from SPF, GF, and CONV mice (n = 3–5 mice/group).

Data information: Data are represented as means ± SD. $^*P < 0.05$; $^{**}P < 0.01$ versus WT by two-tailed unpaired Student's t-test (B, D and F) and two-way ANOVA with Bonferroni *post hoc* analysis (H and I). $^{**}P < 0.01$ versus SPF mice; $^{\#}P < 0.05$; $^{\#\#}P < 0.01$ versus GF mice by one-way ANOVA with Bonferroni's multiple comparison test (J and K).

macrophages were incubated with differently specific agonists to various subtypes of TLRs *ex vivo* (Fig EV4A and B). Intriguingly, VEGF-C secretion increased only in the TLR1/2-activated macrophages, although TNFα and IL-6 mRNA levels were also increased by the other specific TLR agonists (Appendix Fig S8). Because TLR1/2 is largely activated by Gram-positive-derived products, we orally administered vancomycin, which exclusively targets Gram-positive bacteria [49,50], to mice to address whether depletion of vancomycin-sensitive microbes is sufficient to damage lacteal integrity (Fig EV4C and D). The treatment caused lacteal shortening by 15% in the jejunum and ileum. These data imply that the narrow spectrum of gut microbiota sensitive to vancomycin, at least in part, contribute to the lacteal integrity.

To further test whether gut microbiota directly stimulates lacteals for maintenance, we specifically ablated MyD88 in LECs using $MyD88^{i\Delta LEC}$ mice, which were generated by crossing Prox1-$CreER^{T2}$ and $MyD88^{fl/fl}$ animals (Fig A). We failed, however, to detect any differences in lacteals between $MyD88^{i\Delta LEC}$ mice and their WT littermates (Fig B and C), implying that direct stimulation of the microbial component on LECs via MyD88 is barely associated with lacteal integrity.

Discussion

In this study, we reveal that gut microbiota not only maintains lacteal integrity in adult mice but also facilitates postnatal lacteal maturation. Mechanistically, VEGF-C secreted from villus macrophages upon MyD88-dependent recognition of microbes and their products is a main factor in lacteal integrity. In contrast, the gut microbiota does not seem to significantly influence lymphatic vessels distributed in other organs.

One of the intriguing findings of this study is that the degree of lacteal regression was proportionally correlated with the extent of populated gut microbiota in different regions of the small intestine. Indeed, the lacteal regressions triggered by the germ depletion were detected only in jejunum and ileum but not duodenum. Similarly, gut microbiota governs development of the enteric nervous system only in the jejunum and ileum but not the duodenum [28,51]. These regional differences could be derived from differences in microbial density and composition [15]. Moreover, the lacteal regression in jejunum was not evident during the postnatal period, at which time the diversity and population of the gut microbiota have not yet been fully enriched [34,52]. Thus, the enriched gut microbiota endows its unique microenvironment particularly for maintaining lacteal integrity.

Lymphatic vessels distributed in major organs have remarkable plasticity and heterogeneity, reflecting their functional specialization to regulate the organ-specific microenvironment [53–55]. In particular, the skin dermis and mucosal membrane for most organs are rich in lymphatic vessels [56]. Of note, population, type, and roles of microbiota are also organ-specific [53,54,57]. Moreover, the skin epidermis and mucosal membrane for most organs are rich in different microbiota [58]. It would be interesting to understand how normal flora in different organs regulate the function and structure of lymphatic vessels in an organ-specific manner.

We noted that lacteal defect in the GF mice is thought to be mainly due to reduced VEGF-C expression rather than active cell death, supporting the importance of VEGF-C signaling in maintaining lacteal integrity as previously described [2,12]. In the present study, either complete inactivation of VEGFR3 in $VEGFR3^{i\Delta LEC}$ mice or < 50% reduction of VEGF-C in ABX-treated mice was sufficient to reduce lacteal length to the same extent. While VEGF-C retains its dose-dependent effect on the lymphangiogenesis after birth [59], haploinsufficiency of VEGFR3 did not show distinct phenotypes, compared to the WT mice [60]. Therefore, 50% reduction of VEGF-C mRNA level should not be equal to 50% reduction of VEGFR3 mRNA level. Moreover, although VEGFR3 is a major receptor of VEGF-C, VEGF-C also binds to VEGFR2 to regulate lymphangiogenesis [61], eliciting functional redundancy with VEGFR3. Considering this complex mode of action of VEGF-C and its cognate receptors, the lacteal phenotypes in ABX-treated and $VEGFR3^{i\Delta LEC}$ mice seem quite reasonable. Based on the observation from $VEGFR3^{i\Delta LEC}$ mice, we believe that VEGF-C–VEGFR3 axis crucially regulates the lacteal integrity along the entire length of intestinal tract, including the duodenum. We speculate that other factors, rather than gut microbiota, might regulate tissue VEGF-C level in more proximal part of intestine (e.g., duodenum), since the abundance of microbiota is exponentially less in this segment of intestine than in the jejunum and ileum, and depletion of gut microbiota would only minimally alter the microenvironment in the duodenum. Especially, we unveiled that villus macrophages are key neighboring cells for supporting lacteal integrity under homeostatic, non-inflammatory conditions by secreting VEGF-C. Longitudinal SMCs surrounding

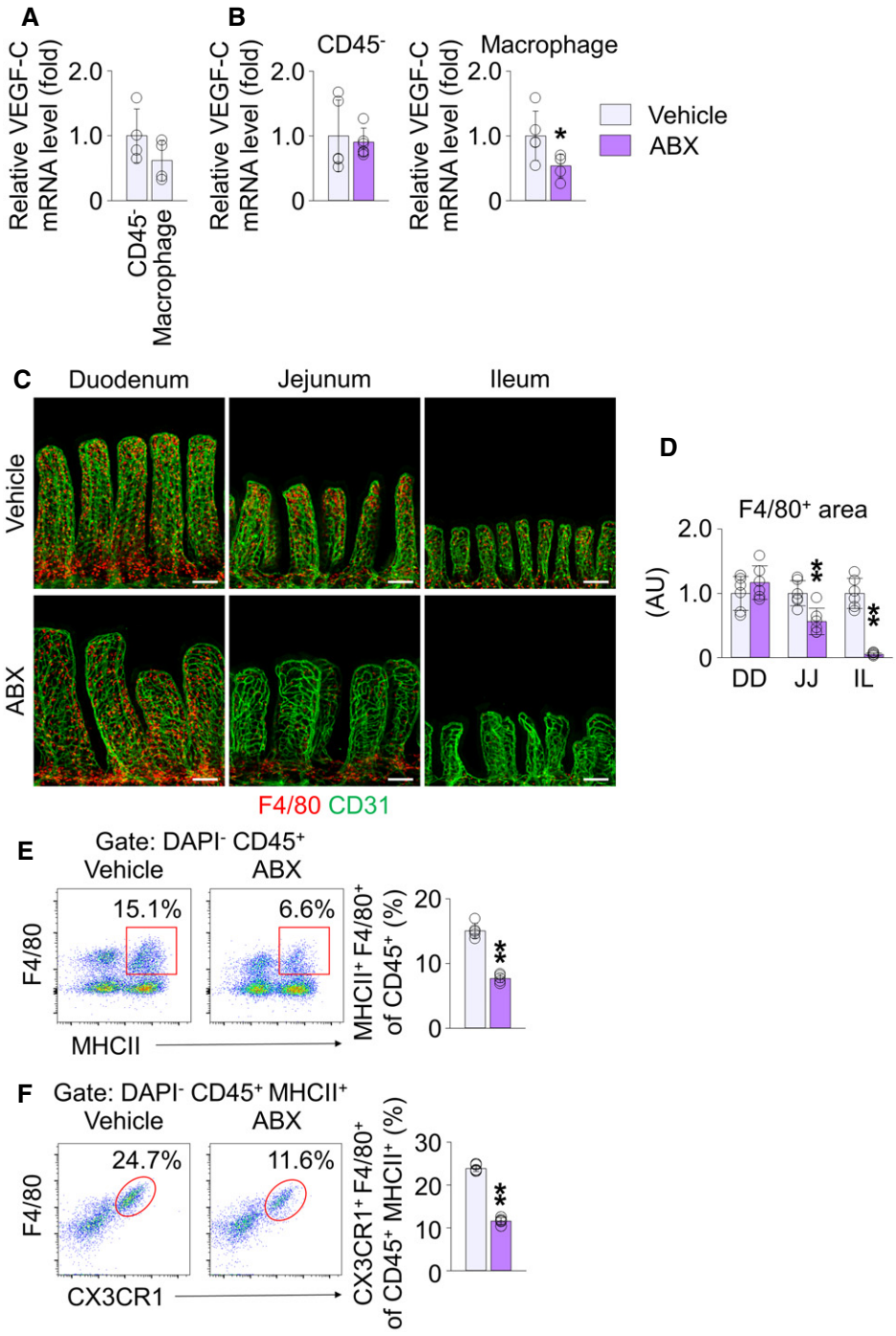

Figure 6. Depletion of gut microbiota reduces both VEGF-C transcription of macrophages and number of macrophages in intestinal villi.

A Comparison of mRNA levels of VEGF-C in sorted CD45$^-$ stromal cells and CD45$^+$ MHCII$^+$ F4/80$^+$ macrophages from jejunum and ileum of vehicle-treated mice. The mean of transcription levels of VEGF-C in CD45$^-$ stromal cells was normalized to 1, and the relative levels in macrophages were presented as fold change (n = 4 mice/group).

B Comparisons of VEGF-C transcription level in CD45$^-$ stromal cells (left) and CD45$^+$ MHCII$^+$ F4/80$^+$ macrophages (right) in jejunum and ileum of vehicle- and ABX-treated mice. The mean of transcription levels of VEGF-C in vehicle-treated mice was normalized to 1, and the relative levels in ABX-treated mice were presented as fold change (n = 5–6 mice/group).

C, D Images and comparison of F4/80$^+$ macrophages in the villi of duodenum (DD), jejunum (JJ), and ileum (IL) from vehicle- or ABX-treated mice. Each dot indicates mean value of five sites in a mouse (n = 6 mice/group). AU, arbitrary unit. Scale bars, 100 μm.

E, F Representative flow cytometric analysis and comparison of MHCII$^+$ F4/80$^+$ macrophage gated on DAPI$^-$ CD45$^+$ cells (E) or CX3CR1$^+$ F4/80$^+$ macrophage gated on DAPI$^-$ CD45$^+$ MHCII$^+$ cells (F) macrophage gated on DAPI$^-$ CD45$^+$ cells from jejunum and ileum of vehicle- and ABX-treated mice (n = 5 mice/group).

Data information: Data are represented as means ± SD. *P < 0.05, **P < 0.01 versus vehicle-treated mice by two-tailed unpaired Student's t-test.

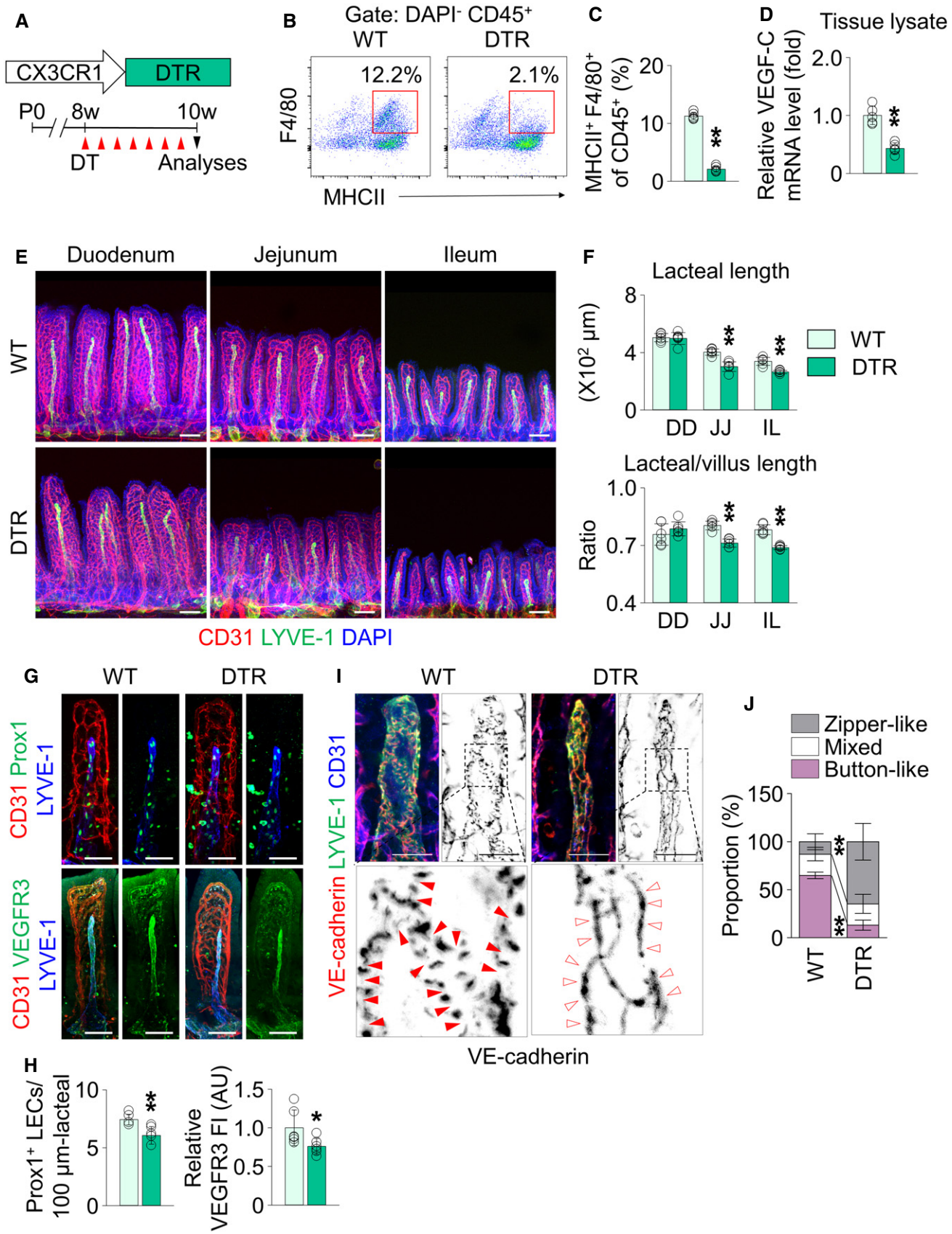

Figure 7.

Figure 7. Depletion of CX3CR1$^+$ macrophages causes lacteal regression.

A Diagram for ablation of CX3CR1$^+$ macrophages using CX3CR1-DTR (DTR) mice. DT, diphtheria toxin.

B, C Representative flow cytometric analysis and comparison of MHCII$^+$ F4/80$^+$ macrophage gated on DAPI$^-$ CD45$^+$ cells from jejunum and ileum of WT and DTR mice (n = 5 mice/group).

D Comparison of mRNA levels of VEGF-C in the whole tissue of jejunum and ileum from WT and DTR mice (n = 5 mice/group).

E, F Images and comparisons of absolute and relative lacteal lengths in duodenum (DD), jejunum (JJ) and ileum (IL) of WT and DTR mice. Each dot indicates mean value of 5–10 villi in a mouse (n = 6 mice/group). Scale bars, 100 μm.

G, H Images and comparisons of number of Prox1$^+$ LECs within initial 100 μm portion (upper) and VEGFR3 expression (lower, presented as relative fluorescent intensity (FI)) in CD31$^+$/LYVE-1$^+$ lacteals of jejunum from WT and DTR mice. Each dot indicates mean value of 5–10 villi in a mouse (n = 6 mice/group). AU, arbitrary unit. Scale bars, 100 μm.

I, J Images and comparison of proportions of each VE-cadherin LEC junctions in CD31$^+$/LYVE-1$^+$ lacteals in jejunum between WT and DTR mice. Button-like (red arrowheads) and zipper-like (open arrowheads) junctions are indicated in each magnified box in below (n = 6 mice/group, 5–10 villi/mouse). Scale bars, 25 μm.

Data information: Data are represented as means ± SD. *P < 0.05, **P < 0.01 versus WT by two-tailed unpaired Student's t-test (C, D, F, and H) and by two-way ANOVA with Bonferroni *post hoc* analysis (J).

lacteals are the source of VEGF-C for lacteal integrity [12]. While the contribution of VEGF-C originated from SMCs is indispensable throughout the entire length of intestine, SMCs seem to have regulatory factors other than gut microbiota regarding VEGF-C production. To define the differential regulatory mechanisms of VEGF-C production and the relative contribution of VEGF-C from different sources to the lacteal integrity would also be interesting questions further to be dissected.

In the present study, we highlighted how villus macrophages are involved in lacteal integrity. Features of villus macrophages are dynamically changed depending on gut microbiota and food antigens and play key roles in regulating intestinal immune tolerance and mucosal homeostasis [21,44,62–66]. For instance, the reduction in the number of CD45$^+$ MHCII$^+$ F4/80$^+$ macrophages and VEGF-C mRNA levels in sorted villus macrophages of MyD88$^{\Delta MP}$ mice was in line with the previous report [62]. Sensing of commensal microbes via MyD88 in the macrophages leads to the immune homeostasis in the intestine by stimulating a subset of innate lymphoid cells, which in turn regulates the number and function of mononuclear phagocytes in the intestine. Moreover, our findings indicate that stimulation of specific TLR subtypes significantly induces VEGF-C production in villus macrophages. Therefore, the recognition of microbial component via the TLR-MyD88 complex is a critical upstream signal for VEGF-C production in villus macrophages for lacteal integrity.

For lipid absorption, lacteals take up chylomicrons, which are repackaged by enterocytes after absorbing dietary lipid from intestinal lumen. In this study, the appearance of TG and FFA in the serum has been used as a method of monitoring the kinetics of lipid transport into blood [13]. However, because alterations in gut microbiota may cause undesirable effects on lipid digestion prior to reaching the lacteals [67], the serum level alone cannot be an appropriate functional indicator of lipid drainage. In order to directly compare the entry process of repackaged chylomicron into the lacteal between two groups, we performed intravital imaging technique [11], demonstrating that residual signal of BODIPY-FA, which failed to enter the lacteal, was significantly more accumulated in lamina propria compartment of ABX-treated mice. This result led us to conclude that drainage of absorbed lipids is functionally compromised in ABX-induced germ-depleted animals.

Such lacteal dysfunction is attributed to the structural defects. Beyond lacteal shortening resulting in the reduction of lacteal surface area from villi throughout the affected region, the microbiota depletion converted the discontinuous, button-like junction to the continuous, zipper-like junction of the lacteals. It is widely accepted that the ease of access of large molecules to the lymphatic vasculature is primarily due to the specialized button-like junctions in initial lymphatics, and that zipper-like junctions are less penetrable [32]. However, no clear ultrastructural evidence explained how button-like junctions in lacteals could facilitate the transport of digested lipid particles. Because of the huge time gap between the ultrastructural study [68] and the characterization of junctional patterns in lacteals [13], the functional significance of ultrastructurally open flaps was not translated into the appearance of VE-

Figure 8. Deletion of MyD88 in macrophages reduces VEGF-C expression in macrophages of villi, leading to lacteal regression.

A Diagram for deletion of MyD88 in macrophages using MyD88$^{\Delta MP}$ mice.

B, C Representative flow cytometric analysis and comparison of MHCII$^+$ F4/80$^+$ macrophage gated on DAPI$^-$ CD45$^+$ cells from jejunum and ileum of WT and MyD88$^{\Delta MP}$ mice (n = 5 mice/group).

D Comparisons of mRNA levels of VEGF-C in sorted MHCII$^+$ F4/80$^+$ macrophages from jejunum and ileum of WT and MyD88$^{\Delta MP}$ mice. The mean of transcription levels of VEGF-C in WT mice was normalized to 1, and the relative level in MyD88$^{\Delta MP}$ mice was presented as fold change (n = 5 mice/group).

E, F Images and comparisons of absolute and relative lacteal lengths in duodenum (DD), jejunum (JJ) and ileum (IL) of WT and MyD88$^{\Delta MP}$ mice. Each dot indicates mean value of 5–10 villi in a mouse (n = 6 mice/group). Scale bars, 100 μm.

G, H Images and comparisons of number of Prox1$^+$ LECs within initial 100 μm portion (upper) and VEGFR3 expression (lower, presented as relative fluorescent intensity (FI)) in CD31$^+$/LYVE-1$^+$ lacteals of jejunum from WT and MyD88$^{\Delta MP}$ mice. Each dot indicates mean value of 5–10 villi. Each dot indicates mean value of 5–10 villi in a mouse (n = 6 mice/group). AU, arbitrary unit. Scale bars, 100 μm.

I, J Images and comparison of proportions of each VE-cadherin LEC junctions in CD31$^+$/LYVE-1$^+$ lacteals in jejunum between WT and MyD88$^{\Delta MP}$ mice. Button-like (red arrowheads) and zipper-like (open arrowheads) junctions are indicated in each magnified box in below (n = 6 mice/group, 5–10 villi/mouse). Scale bars, 25 μm.

Data information: Data are represented as means ± SD. *P < 0.05, **P < 0.01 versus WT by two-tailed unpaired Student's t-test (C, D, F, and H) and two-way ANOVA with Bonferroni *post hoc* analysis (J).

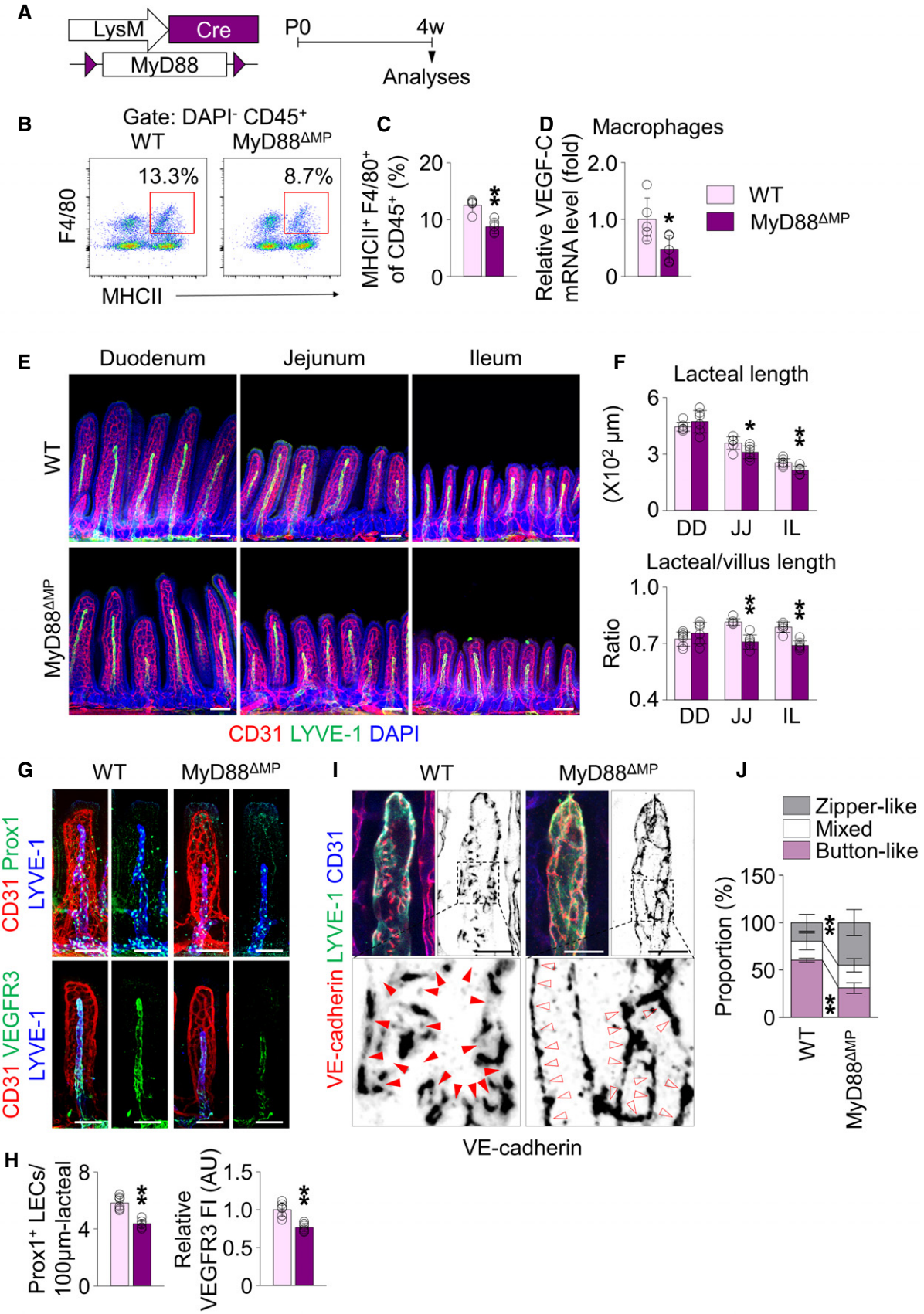

Figure 8.

cadherin junction in the lacteal. Here, using transmission electron microscopic analysis, we demonstrated that dietary lipid is transported into the lacteal lumen both via open junctions between LECs (paracellular pathway) and via cellular uptake of chylomicron and excretion into the lumen (transcellular pathway), while only the latter is working in ABX-treated mice, which findings present a mechanistic insight how button-like junctions could facilitate the lipid transport via ultrastructurally open junctions between LECs in healthy lacteals. Collectively, we assume that structural defect in the lacteal length and LEC junctions resulting from germ depletion synergistically opposes the optimal function of lacteals in germ-depleted mice.

Materials and Methods

Mice

Animal care and experimental procedures were performed under the approval from the Institutional Animal Care and Use Committee of KAIST (IACUC-17-51) and POSTECH (POSTECH-2014-0030-C1). WT, RiboTag [69] (Jackson stock number 011029), LysM-Cre [48] (Jackson stock number 004781), and Myd88$^{fl/fl}$ [47] (Jackson stock number 009108) mice on C57BL/6J background were purchased from Jackson Laboratory. Prox1-CreER^{T2} [37], VEGFR3$^{fl/fl}$ [36], and CX3CR1-DTR mice [45] were transferred and bred in our SPF animal facilities at KAIST. To induce Cre activity in CreER^{T2} mice, tamoxifen (100 mg/kg mouse, Sigma-Aldrich) in corn oil was subcutaneously injected in 8-week-old mice every other day for three times. For macrophage deletion, DT (Sigma-Aldrich) was administered via intraperitoneal route for 2 weeks in CX3CR1-DTR mice as previously described [45]. DT was also administered to the WT mice, as a control group. GF C57BL/6 mice [22] were raised in sterile flexible film isolators (Class Biological Clean Ltd, USA) and maintained in the animal facility of POSTECH Biotech Center in accordance with institutional ethical guideline. For conventionalization of GF mice, 4-week-old GF mice were co-housed with conventional SPF mice for additional 4 weeks before analyses, as previously described [70]. Alternatively, to quantify the alterations in tissue VEGF-C level during early period after conventionalization, CONV mice were sacrificed on day 5 after conventionalization. Male and female mice were not distinguished in pup study, while only male mice were used in adult experiments. All mice were fed with free access to a standard diet (PMI Lab diet) and water.

Treatment of mice with antibiotics

To deplete gut microbiota, a cocktail of antibiotics dissolved in 2% sucrose (ABX) was orally administered for 4 weeks prior to experiments unless otherwise indicated, at the following concentrations: ampicillin, 0.5 mg/ml (Sigma-Aldrich); vancomycin, 0.25 mg/ml (Pfizer); metronidazole, 0.5 mg/ml (Sigma-Aldrich); neomycin, 0.5 mg/ml (A.G. Scientific). Control mice received 2% sucrose without antibiotics. To investigate the effect of postnatal microbial expansion on the lacteal maturation, ABX was given to WT mice from 4 weeks before mating. ABX administration was maintained after the mating and birth of pups and was continued until the sacrifice of their pups on P7, P14, and P28.

Feces culture and colony-forming unit measurement

Feces were collected in a tube and were diluted with 10-weight volume of PBS. The tube was vigorously vortexed. Then, the samples were centrifuged for 10 min at 800 rpm. The supernatant was serially diluted to 10^{-2} to 10^{-5} folds and then was streaked with cell spreader on a LB agar plate. After overnight incubation at 37°C, colony-forming unit was measured.

Immunohistochemical staining

Small intestine whole-mount was performed as previously described [71], with minor modifications. Briefly, 4% paraformaldehyde (PFA) in PBS was perfused with cardiac puncture in anesthetized mice. Small intestine was harvested and was longitudinally cut to expose the lumen. After washing the luminal contents with ice-cold PBS, intestines were pinned on silicon plates with villi side up. Intestine samples were then post-fixed in 4% PFA in PBS for 2 h at 4°C. Samples were briefly washed with ice-cold PBS for 3 times and were subsequently washed with 10% sucrose in PBS for 2 h and with 20% sucrose, 10% glycerol in PBS overnight at 4°C. Following the blocking with 5% goat or donkey serum in 0.3% Triton X-100 in PBS (0.3% PBS-T) for 1 h, primary antibodies diluted in the blocking solution were incubated with intestine samples overnight at 4°C. After washing with ice-cold 0.3% PBS-T, secondary antibodies were diluted in the blocking solution, followed by overnight incubation at 4°C. Then, samples were washed with ice-cold 0.3% PBS-T and were stained with DAPI. Under stereoscopic field, stained samples were longitudinally dissected with micro-scissors to make a strip with a width of one or two villi, which was laid down flat on the slide glass for mounting with cover glass. Ear skin, trachea, and diaphragm and inguinal LNs were harvested and were fixed with 1% PFA in PBS for 1 h at 4°C. For cryosection, inguinal LNs were embedded in tissue freezing medium (Leica). Following the blocking with 5% goat or donkey serum in 0.3% PBS-T for 1 h at 4°C, the whole-mounted or cyrosectioned tissues were incubated with primary and secondary antibodies and were mounted. The following primary antibodies were used in the immunostaining: anti-CD31 (hamster monoclonal, clone 2H8, Millipore); anti-CD31 (rat monoclonal, clone MEC 13.3, BD Bioscience; Cy3-conjugated anti-αSMA (mouse monoclonal, clone 1A4, Sigma-Aldrich); anti-F4/80 (rat monoclonal, clone BM8, BioLegend); anti-Prox1 (rabbit polyclonal, ReliaTech); anti-VEGFR2 (goat polyclonal, R&D); anti-VEGFR3 (goat polyclonal, R&D); anti-VE-cadherin (goat polyclonal, R&D); anti-LYVE-1 (rabbit polyclonal, AngioBio); and anti-LYVE-1 (rat monoclonal, clone ALY7, eBioscience). Alexa 488-, Alexa 594-, and Alexa 647-conjugated secondary antibodies were purchased from Jackson ImmunoResearch. Images were acquired using a Zeiss LSM 800 or 880 confocal microscope equipped with argon and helium–neon lasers (Carl Zeiss).

HDLEC culture and immunocytochemistry

Primary LECs were isolated and cultured as previously described [72] with the approval of the University of Southern California Institutional Review Board (Y.K. Hong). In brief, the cells were cultured in endothelial growth medium (EGM2-MV, Lonza) and incubated in a humidified atmosphere of 5% CO_2 at 37°C. The passages of

HDLECs up to 10 were used for *in vitro* experiments. For immunocytochemistry, HDLECs cultured in an 8-well chamber (Lab-Tek, Thermo Fisher Scientific) were fixed with 1% PFA in PBS for 10 min at room temperature (RT), and permeabilized with 0.5% PBS-T for 5 min at RT. The sample was blocked with 5% donkey serum in 0.1% PBS-T for 30 min at RT. After overnight incubation with primary antibodies at 4°C, cells were then incubated with secondary antibodies in the dark for 1 h at RT. Samples were mounted with DAPI-containing mounting medium (DAKO). Primary antibodies used were anti-VE-cadherin (mouse monoclonal, clone BV6, Millipore), anti-Prox1 (goat polyclonal, R&D systems), and anti-caspase-3 (rabbit polyclonal, Cell Signaling Technology). Alexa 488-, Alexa 594-, and Alexa 647-conjugated secondary antibodies were purchased from Jackson ImmunoResearch. Images were acquired using a Zeiss LSM 800 or 880 confocal microscope equipped with argon and helium–neon lasers (Carl Zeiss).

Morphometric analyses

Morphometric analyses were made by photographic analysis using LSM Image Browser (Carl Zeiss), ImageJ software (NIH) or Imaris (Bitplane). To analyze the lacteal structure, we measured the lengths of blood capillary, lacteal, and villus itself from each villus (defined as "absolute lengths"). Since the lacteal length is highly variable, but tend to be proportional to the villus or capillary length, we also calculated the lacteal/villus or lacteal/capillary length ratio (defined as "relative lengths"), which parameters are proven to be relatively even along the entire length of intestine [13]. Junctional pattern in lacteals was defined as previously described [39], with minor modifications. Briefly, button-like junction was defined as discontinuous junctions that are not parallel to cell–cell borders and are associated with an oak leaf cell shape. Zipper-like junctions were defined as continuous junctions at cell–cell borders, accompanied by elongated cell shapes (Appendix Fig S1B). Junctions that do not fully match to either patterns were defined as mixed type. Lacteals from 5 to 10 villi in a mouse were randomly analyzed to determine predominant LECs junctional pattern. The proportion of junctional pattern in lacteals were compared between the groups. To determine blood or lymphatic vessel densities, $CD31^+$ or LYVE-1^+ areas were measured, respectively, in five 0.0265 mm^2 fields per samples and were presented as relative values divided by its control area. The number of Prox1^+ LECs in lacteals was counted from the initial 100 μm of LYVE-1^+ lacteal area. To determine the relative expression of VEGFR2 and VEGFR3, mean fluorescent intensities (MFI) measured in five 0.0265 mm^2 fields per samples was divided by CD31 MFI and was presented as relative values divided by its control. The density of SMCs or macrophages was measured by αSMA^+ or F4/80^+ area from five 0.0265 mm^2 fields per samples, was presented as relative values divided by its control area. The Prox1 expression in HDLECs was determined by MFI and was presented as relative values divided by its control. The total nucleated and caspase-3^+ HDLECs were counted from randomly selected five 0.0265 mm^2 areas, and the percentage of caspase-3^+ HDLECs was calculated.

Intravital microscopy of lipid clearance from lamina propria

For intravital microscopy, we used same method as previously described [11]. BODIPY-FA (0.1 mg/ml, BODIPY FL C16, Invitrogen) was dissolved in 10% 2.5% DMSO solution (Sigma-Aldrich). For fluorescent labeling of lacteals *in vivo*, we intravenously injected 0.75 mg/kg of anti-LYVE-1 antibody (rat monoclonal, Clone 223322, R&D) conjugated with Alexa 647 (Invitrogen) at 12 h before the imaging. Before the imaging, the mice were deprived of food for 12 h. Mice were anesthetized by intramuscular injection of Zoletil (20 mg/kg) and xylazine (11 mg/kg) mixture. About 8 cm of the proximal jejunum was exteriorized and placed in an imaging chamber where moisture and temperature (36–38°C) were maintained during the imaging. About 1.5 cm of the intestine was surgically opened along the anti-mesenteric border. A cover glass was placed on the exposed lumen to obtain a clear view of villi. The intravital imaging was performed over five sessions. The villi were first imaged before the BODIPY-FA supply to observe the villi at 0 min. Then, 30 μl of BODIPY-FA was supplied once before the second imaging session to observe the initial BODIPY-FA absorption at 1 min. Next, the BODIPY-FAs were supplied in excess of three times with 2-min intervals before the third imaging session at 16 min. Finally, we could observe the BODIPY-FA clearing through lacteals at 26 and 36 min. In order to supply the BODIPY-FA, the cover glass was temporarily removed from the intestinal lumen and the BODIPY-FA was provided 1 and 6 min before the second and third imaging sessions, respectively, to facilitate rapid spontaneous drainage of BODIPY-FA before mounting again with the cover glass. We used a home-built video-rate laser-scanning confocal microscope [11]. Two continuous-wave lasers emitting at 488 nm (MLD, Coherent) and 640 nm (Cube, Coherent) were used as excitation sources for fluorescence imaging. Two bandpass filters (FF01-525/50 and FF01-685/40, Semrock) were used for detection of fluorescent signals. Axial resolution below 4 μm was acquired with 100 μm pinhole and 60× objective lens (LUMFLN, water immersion, NA 1.1, Olympus). Images (512 × 512 pixels) were obtained at a frame rate of 30 Hz. For the signal-to-noise ratio enhancement of the image, we performed averaging the noise over 90 frames after post-processing the real-time images (30 frames/s) by removing the motion artifact generated from peristalsis with a custom-written MATLAB program. For measuring the average fluorescent intensity in the lamina propria, we used ImageJ software (NIH).

Transmission electron microscopy

Following overnight starvation, the mice were fed with 300 μl of corn oil (Sigma-Aldrich). Jejunum harvested 2 h after corn oil feeding were fixed with 2.5% glutaraldehyde (Ted Pella) in PBS overnight and were post-fixed for 2 h with 1% OsO4 in 0.1 M cacodylate buffer (pH 7.2). Tissue was dehydrated with ethanol series and propylene oxide, and the tissues were embedded in Embed-812 (EMS). Following resin polymerization, the tissues were sectioned using an ULTRACUT UC7 ultramicrotome (Leica, Austria) and mounted on Formvar-coated slot grid. After staining with 4% uranyl acetate and lead citrate, the sections were observed using a Tecnai G2 Spirit Twin transmission electron microscope (FEI).

Lipid absorption test

For lipid absorption test, 300 μl of corn oil (Sigma-Aldrich) was administered to the stomach of mice using a feeding tube after being

fasted for 6 h. Blood was sampled at 0, 1, 2, and 3 h after the oil administration by tail vein collection in EDTA-coated tubes. TG and FFA analysis was performed on FUJI DRI-CHEM 7000i (Fuji Film) and VetTest Chemistry analyzer (IDEXX Lab), respectively.

Lymph sampling from thoracic duct

To identify lymphatic vessels, mice were given 300 μl of corn oil (Sigma-Aldrich) 30 min before the procedure. Then, mice were anesthetized with isoflurane using a facial mask. In right-decubitus position, the abdomen was opened with the left subcostal incision, to mobilize spleen, bowel, and kidney to identify the aorta after dorsal parietal peritoneal dissection. The thoracic duct was observed behind the aorta. The EDTA-flushed PE-10 polyethylene tube was passed through the lumbar muscles below the rib cage using 20-gauge cannula. The thoracic duct was punctured with fine microforceps, and the PE-10 tube was inserted. Lymph was collected in EDTA-flushed 30-gauge insulin syringe.

Preparation of stromal cells from small intestine lamina propria

Intestine was harvested, cut into small pieces, and digested as previously described [73]. Briefly, we opened gut fragments longitudinally, cut them into 2 cm pieces, and incubated for 20 min at 37°C in DMEM containing 10 mM EDTA under gentle agitation (200 rpm). We washed tissue pieces by vortexing quickly with PBS until obtaining a clear supernatant devoid of epithelial cells. We subsequently cut gut pieces into 1-mm fragments and incubated for 20 min at 37°C in a dissociation mix composed of 10 ml DMEM, Liberase TL (1 Wunsch unit/ml, Roche) and DNase I (1 U/ml, Invitrogen). To help dissociation, we gently agitated tissue pieces by pipetting up and down. We harvested supernatants and added 1 volume of DMEM containing 10% bovine serum while adding 10 ml of fresh dissociation mix to the remaining tissue pieces. We repeated this step three times for a total 60 min. After completion of the three cycles, we washed the cellular suspension twice with DMEM in order to eliminate floating debris and filtered through a 70-μm strainer.

Flow cytometry and cell sorting

The digested cells were incubated with CD45-microbead (Miltenyi Biotec) for 15 min. After washing the cell incubate, cells were positively or negatively selected using MACS (Miltenyl). The cells were incubated for 30 min with the following antibodies in FACS buffer (5% bovine serum in PBS): anti-CD45 (clone 30-F11, eBioscience), anti-F4/80 (clone BM8, BioLegend), anti-MHCII (clone M5/114.15.2, BioLegend), anti-CX3CR1 (Clone SA011F11, BioLegend). Dead cells were excluded using DAPI staining (Sigma-Aldrich). After several washes, cells were analyzed by FACS Canto II (BD Biosciences) and acquired data were further evaluated by using FlowJo software (Treestar). Cell sorting was performed by FACS Aria II (Becton Dickinson).

Stimulation of primary intestinal macrophages with specific TLR agonists

The same number of sorted intestinal macrophages was incubated in a well of 384-well plate with 50 μl of RPMI 1640 media supplemented with 10% bovine serum. The following TLR agonists were treated for 12 h (all from InvivoGen): palmitoyl-3-cysteine-serine-lysine-4 (1 μg/ml), poly(I-C) (10 μg/ml), lipopolysaccharide (5 μg/ml), flagellin (0.1 mg/ml), or endotoxin-free bacterial DNA (10 μg/ml).

Measurement of VEGF-A and VEGF-C protein levels

Tissue or culture supernatant protein level of VEGF-A and/or VEGF-C was measured using Milliplex MAP kit (Millipore), according to the manufacturer's instruction. Briefly, 10 mg of intestinal tissue lysate or culture supernatants (25 μl) was incubated with VEGF-A- or VEGF-C-specific capture antibodies coupled with fluorescent beads in a 96-well plate for overnight at 4°C. After three times washing, biotinylated detector antibodies were added, followed by streptavidin–phycoerythrin incubation for 1 h at RT. Data were acquired using Luminex™ 200 system instrument and analyzed with Luminex xPONENT software (Thermo Fisher). VEGF-A and VEGF-C levels were quantified using a logistic regression curve derived from the reference cytokine concentration standards supplied by manufacturer.

mRNA isolation using RiboTag method

RiboTag mouse was crossed to Prox1-CreER^{T2} to isolate the LEC-specific mRNA. To induce Cre activity in CreERT2 mice, tamoxifen (100 mg/kg mouse, Sigma-Aldrich) in corn oil was subcutaneously injected in 8-week-old mice every other day for three times. 2 weeks after induction of Cre recombinase, the mice were sacrificed to isolate polysome-bound mRNAs of LECs in the intestine, with minor modifications from previously described method [69]. Briefly, intestine was harvested, opened longitudinally, and cut into 2-cm pieces. Tissues were incubated for 20 min at 37°C in DMEM containing 10 mM EDTA under gentle agitation (200 rpm). Tissue pieces were washed by vortexing quickly with PBS until obtaining a clear supernatant devoid of epithelial cells. The samples were immediately snap frozen. Then, polysome buffer (50 mM Tris, pH 7.5, 100 mM KCl, 12 mM $MgCl_2$, 1% Nonidet P-40, 1 mM DTT, 200 U/ml RNasin, 1 mg/ml heparin, 100 μg/ml cycloheximide, and 1× protease inhibitor mixture) was added to each sample and homogenized using Precellys lysis kit (Bertin). For immunoprecipitation against hemagglutinin, anti-hemagglutinin antibody-conjugated magnetic beads (MBL, M180-11) were added to the supernatant after centrifugation for 10 min at 13,500 *g* 4°C and incubated on a rotating shaker at 4°C overnight. Beads were washed for four times with high-salt buffer (50 mM Tris, pH 7.5, 300 mM KCl, 12 mM $MgCl_2$, 1% Nonidet P-40, 1 mM DTT, and 100 μg/ml cycloheximide) and resuspended in 350 μl of RLT plus buffer with β-mercaptoethanol. Total RNAs were extracted using the RNA isolation mentioned in methods.

Real-time PCR

Total RNA was isolated from sorted cells using RNeasy Micro kit (Qiagen) according to the manufacturer's instructions. For investigation of mRNA, total RNA was reverse transcribed using iScript Reverse Transcription Supermix (Bio-Rad). Real-time RT–PCR was performed in triplicate using SYBR Green PCR Master

Mix (Applied Biosystems) and run on QuantiStudio3 systems (Applied Biosystems) using primers listed in the Appendix Table S1. The PCR conditions for mRNA quantification were 95°C for 10 min, followed by 40 cycles with denaturation at 95°C for 10 s and annealing and extension at 60°C for 1 min. All data were normalized to *Gapdh*.

Statistics

No statistical method was used to predetermine the sample size. All parameters of genetically modified mice were compared with those of littermate control. Animals or samples were not randomized during experiments and not excluded from analyses. The investigators were not blinded to group allocation during experiments and outcome analyses. Statistical analyses were performed with Prism software (GraphPad Software) using two-tailed unpaired Student's *t*-test, one-way ANOVA with Tukey's multiple comparison test, Dunnett's multiple comparison test or Bonferroni's multiple comparison test, and two-way ANOVA with Bonferroni *post hoc* analyses as indicated. Error bars represent SD or SEM as indicated. Statistical significance was set at $P < 0.05$.

Expanded View for this article is available online.

Acknowledgements
We thank Sujin Seo, Hyun-Tae Kim, and Eun-Soon Lee for their technical assistances. This study was supported by the Institute for Basic Science funded by the Ministry of Science, ICT and Future Planning, Korea (IBS-R025-D1-2015, GYK).

Author contributions
SHS, SHJ, and GYK designed the research studies; SHS, JHS, KC, SPH, and SHJ conducted the experiments and analyzed the data; TM, KSK, KA, and CDS provided the mice, and SHS, JHS, and GYK generated the figures and wrote and edited the manuscript; and GYK directed and supervised the project.

Conflict of interest
The authors declare that they have no conflict of interest.

References

1. Miller MJ, McDole JR, Newberry RD (2010) Microanatomy of the intestinal lymphatic system. *Ann N Y Acad Sci* 1207(Suppl 1): E21 – E28
2. Bernier-Latmani J, Petrova TV (2017) Intestinal lymphatic vasculature: structure, mechanisms and functions. *Nat Rev Gastroenterol Hepatol* 14: 510 – 526
3. Vetrano S, Borroni EM, Sarukhan A, Savino B, Bonecchi R, Correale C, Arena V, Fantini M, Roncalli M, Malesci A *et al* (2010) The lymphatic system controls intestinal inflammation and inflammation-associated colon cancer through the chemokine decoy receptor D6. *Gut* 59: 197 – 206
4. Van Kruiningen HJ, Colombel J-F (2008) The forgotten role of lymphangitis in Crohn's disease. *Gut* 57: 1 – 4
5. Jang JY, Koh YJ, Lee SH, Lee J, Kim KH, Kim D, Koh GY, Yoo OJ (2013) Conditional ablation of LYVE-1+ cells unveils defensive roles of lymphatic vessels in intestine and lymph nodes. *Blood* 122: 2151 – 2161
6. Tonelli F, Giudici F, Liscia G (2012) Is lymphatic status related to regression of inflammation in Crohn's disease? *World J Gastrointest Surg* 4: 228 – 233
7. Rahier J-F, Dubuquoy L, Colombel J-F, Jouret-Mourin A, Delos M, Ferrante M, Sokol H, Hertogh GD, Salleron J, Geboes K *et al* (2013) Decreased lymphatic vessel density is associated with postoperative endoscopic recurrence in Crohn's disease. *Inflamm Bowel Dis* 19: 2084 – 2090
8. Kim H, Kataru RP, Koh GY (2014) Inflammation-associated lymphangiogenesis: a double-edged sword? *J Clin Invest* 124: 936 – 942
9. Jurisic G, Sundberg JP, Detmar M (2013) Blockade of VEGF receptor-3 aggravates inflammatory bowel disease and lymphatic vessel enlargement. *Inflamm Bowel Dis* 19: 1983 – 1989
10. D'Alessio S, Correale C, Tacconi C, Gandelli A, Pietrogrande G, Vetrano S, Genua M, Arena V, Spinelli A, Peyrin-Biroulet L *et al* (2014) VEGF-C-dependent stimulation of lymphatic function ameliorates experimental inflammatory bowel disease. *J Clin Invest* 124: 3863 – 3878
11. Choe K, Jang JY, Park I, Kim Y, Ahn S, Park DY, Hong YK, Alitalo K, Koh GY, Kim P (2015) Intravital imaging of intestinal lacteals unveils lipid drainage through contractility. *J Clin Invest* 125: 4042 – 4052
12. Nurmi H, Saharinen P, Zarkada G, Zheng W, Robciuc MR, Alitalo K (2015) VEGF-C is required for intestinal lymphatic vessel maintenance and lipid absorption. *EMBO Mol Med* 7: 1418 – 1425
13. Bernier-Latmani J, Cisarovsky C, Demir CS, Bruand M, Jaquet M, Davanture S, Ragusa S, Siegert S, Dormond O, Benedito R *et al* (2015) DLL4 promotes continuous adult intestinal lacteal regeneration and dietary fat transport. *J Clin Invest* 125: 4572 – 4586
14. Davis RB, Kechele DO, Blakeney ES, Pawlak JB, Caron KM (2017) Lymphatic deletion of calcitonin receptor-like receptor exacerbates intestinal inflammation. *JCI Insight* 2: e92465
15. Donaldson GP, Lee SM, Mazmanian SK (2016) Gut biogeography of the bacterial microbiota. *Nat Rev Microbiol* 14: 20 – 32
16. Renz H, Brandtzaeg P, Hornef M (2011) The impact of perinatal immune development on mucosal homeostasis and chronic inflammation. *Nat Rev Immunol* 12: 9 – 23
17. Kamada N, Seo SU, Chen GY, Nunez G (2013) Role of the gut microbiota in immunity and inflammatory disease. *Nat Rev Immunol* 13: 321 – 335
18. Littman Dan R, Pamer Eric G (2011) Role of the commensal microbiota in normal and pathogenic host immune responses. *Cell Host Microbe* 10: 311 – 323
19. Hill DA, Artis D (2010) Intestinal bacteria and the regulation of immune cell homeostasis. *Annu Rev Immunol* 28: 623 – 667
20. Hooper LV, Littman DR, Macpherson AJ (2012) Interactions between the microbiota and the immune system. *Science* 336: 1268 – 1273
21. Belkaid Y, Hand TW (2014) Role of the microbiota in immunity and inflammation. *Cell* 157: 121 – 141
22. Kim KS, Hong S-W, Han D, Yi J, Jung J, Yang B-G, Lee JY, Lee M, Surh CD (2016) Dietary antigens limit mucosal immunity by inducing regulatory T cells in the small intestine. *Science* 351: 858 – 863
23. Nicholson JK, Holmes E, Kinross J, Burcelin R, Gibson G, Jia W, Pettersson S (2012) Host-gut microbiota metabolic interactions. *Science* 336: 1262 – 1267
24. Chevalier C, Stojanović O, Colin Didier J, Suarez-Zamorano N, Tarallo V, Veyrat-Durebex C, Rigo D, Fabbiano S, Stevanović A, Hagemann S *et al* Gut microbiota orchestrates energy homeostasis during cold. *Cell* 163: 1360 – 1374
25. Douglas-Escobar M, Elliott E, Neu J (2013) Effect of intestinal microbial ecology on the developing brain. *JAMA Pediatrics* 167: 374 – 379
26. Cryan JF, Dinan TG (2012) Mind-altering microorganisms: the impact of the gut microbiota on brain and behaviour. *Nat Rev Neurosci* 13: 701 – 712

27. Mayer EA, Tillisch K, Gupta A (2015) Gut/brain axis and the microbiota. *J Clin Invest* 125: 926 – 938
28. Yoo BB, Mazmanian SK (2017) The enteric network: interactions between the immune and nervous systems of the gut. *Immunity* 46: 910 – 926
29. Stappenbeck TS, Hooper LV, Gordon JI (2002) Developmental regulation of intestinal angiogenesis by indigenous microbes via Paneth cells. *Proc Natl Acad Sci USA* 99: 15451 – 15455
30. Reinhardt C, Bergentall M, Greiner TU, Schaffner F, Ostergren-Lunden G, Petersen LC, Ruf W, Backhed F (2012) Tissue factor and PAR1 promote microbiota-induced intestinal vascular remodelling. *Nature* 483: 627 – 631
31. Moghadamrad S, McCoy KD, Geuking MB, Sagesser H, Kirundi J, Macpherson AJ, De Gottardi A (2015) Attenuated portal hypertension in germ-free mice: function of bacterial flora on the development of mesenteric lymphatic and blood vessels. *Hepatology* 61: 1685 – 1695
32. Baluk P, Fuxe J, Hashizume H, Romano T, Lashnits E, Butz S, Vestweber D, Corada M, Molendini C, Dejana E *et al* (2007) Functionally specialized junctions between endothelial cells of lymphatic vessels. *J Exp Med* 204: 2349 – 2362
33. Kim KE, Sung HK, Koh GY (2007) Lymphatic development in mouse small intestine. *Dev Dyn* 236: 2020 – 2025
34. Hasegawa M, Osaka T, Tawaratsumida K, Yamazaki T, Tada H, Chen GY, Tsuneda S, Nunez G, Inohara N (2010) Transitions in oral and intestinal microflora composition and innate immune receptor-dependent stimulation during mouse development. *Infect Immun* 78: 639 – 650
35. Abrams GD, Bauer H, Sprinz H (1963) Influence of the normal flora on mucosal morphology and cellular renewal in the ileum. A comparison of germ-free and conventional mice. *Lab Invest* 12: 355 – 364
36. Haiko P, Makinen T, Keskitalo S, Taipale J, Karkkainen MJ, Baldwin ME, Stacker SA, Achen MG, Alitalo K (2008) Deletion of vascular endothelial growth factor C (VEGF-C) and VEGF-D is not equivalent to VEGF receptor 3 deletion in mouse embryos. *Mol Cell Biol* 28: 4843 – 4850
37. Bazigou E, Lyons OT, Smith A, Venn GE, Cope C, Brown NA, Makinen T (2011) Genes regulating lymphangiogenesis control venous valve formation and maintenance in mice. *J Clin Invest* 121: 2984 – 2992
38. Kajiya K, Kidoya H, Sawane M, Matsumoto-Okazaki Y, Yamanishi H, Furuse M, Takakura N (2012) Promotion of lymphatic integrity by angiopoietin-1/Tie2 signaling during inflammation. *Am J Pathol* 180: 1273 – 1282
39. Zheng W, Nurmi H, Appak S, Sabine A, Bovay E, Korhonen EA, Orsenigo F, Lohela M, D'Amico G, Holopainen T *et al* (2014) Angiopoietin 2 regulates the transformation and integrity of lymphatic endothelial cell junctions. *Genes Dev* 28: 1592 – 1603
40. Clavin NW, Avraham T, Fernandez J, Daluvoy SV, Soares MA, Chaudhry A, Mehrara BJ (2008) TGF-beta1 is a negative regulator of lymphatic regeneration during wound repair. *Am J Physiol Heart Circ Physiol* 295: H2113 – H2127
41. Bos FL, Caunt M, Peterson-Maduro J, Planas-Paz L, Kowalski J, Karpanen T, van Impel A, Tong R, Ernst JA, Korving J *et al* (2011) CCBE1 is essential for mammalian lymphatic vascular development and enhances the lymphangiogenic effect of vascular endothelial growth factor-C *in vivo*. *Circ Res* 109: 486 – 491
42. Bui HM, Enis D, Robciuc MR, Nurmi HJ, Cohen J, Chen M, Yang Y, Dhillon V, Johnson K, Zhang H *et al* (2016) Proteolytic activation defines distinct lymphangiogenic mechanisms for VEGFC and VEGFD. *J Clin Invest* 126: 2167 – 2180
43. Becker F, Kurmaeva E, Gavins FN, Stevenson EV, Navratil AR, Jin L, Tsunoda I, Orr AW, Alexander JS, Ostanin DV (2016) A critical role for monocytes/macrophages during intestinal inflammation-associated lymphangiogenesis. *Inflamm Bowel Dis* 22: 1326 – 1345
44. Harvey NL, Gordon EJ (2012) Deciphering the roles of macrophages in developmental and inflammation stimulated lymphangiogenesis. *Vascular Cell* 4: 15
45. Longman RS, Diehl GE, Victorio DA, Huh JR, Galan C, Miraldi ER, Swaminath A, Bonneau R, Scherl EJ, Littman DR (2014) CX(3)CR1(+) mononuclear phagocytes support colitis-associated innate lymphoid cell production of IL-22. *J Exp Med* 211: 1571 – 1583
46. Kawai T, Akira S (2010) The role of pattern-recognition receptors in innate immunity: update on Toll-like receptors. *Nat Immunol* 11: 373 – 384
47. Hou B, Reizis B, DeFranco AL (2008) Toll-like receptors activate innate and adaptive immunity by using dendritic cell-intrinsic and -extrinsic mechanisms. *Immunity* 29: 272 – 282
48. Clausen BE, Burkhardt C, Reith W, Renkawitz R, Forster I (1999) Conditional gene targeting in macrophages and granulocytes using LysMcre mice. *Transgenic Res* 8: 265 – 277
49. Takeuchi O, Hoshino K, Kawai T, Sanjo H, Takada H, Ogawa T, Takeda K, Akira S (1999) Differential roles of TLR2 and TLR4 in recognition of Gram-negative and Gram-positive bacterial cell wall components. *Immunity* 11: 443 – 451
50. Nakanishi Y, Sato T, Ohteki T (2015) Commensal Gram-positive bacteria initiates colitis by inducing monocyte/macrophage mobilization. *Mucosal Immunol* 8: 152 – 160
51. Collins J, Borojevic R, Verdu EF, Huizinga JD, Ratcliffe EM (2014) Intestinal microbiota influence the early postnatal development of the enteric nervous system. *Neurogastroenterol Motil* 26: 98 – 107
52. Jain N, Walker WA (2015) Diet and host-microbial crosstalk in postnatal intestinal immune homeostasis. *Nat Rev Gastroenterol Hepatol* 12: 14 – 25
53. Petrova TV, Koh GY (2017) Organ-specific lymphatic vasculature: from development to pathophysiology. *J Exp Med* 215: 35 – 49
54. Potente M, Makinen T (2017) Vascular heterogeneity and specialization in development and disease. *Nat Rev Mol Cell Biol* 18: 477 – 494
55. Backhed F, Ding H, Wang T, Hooper LV, Koh GY, Nagy A, Semenkovich CF, Gordon JI (2004) The gut microbiota as an environmental factor that regulates fat storage. *Proc Natl Acad Sci USA* 101: 15718 – 15723
56. Choi I, Chung HK, Ramu S, Lee HN, Kim KE, Lee S, Yoo J, Choi D, Lee YS, Aguilar B *et al* (2011) Visualization of lymphatic vessels by Prox1-promoter directed GFP reporter in a bacterial artificial chromosome-based transgenic mouse. *Blood* 117: 362 – 365
57. Ulvmar MH, Makinen T (2016) Heterogeneity in the lymphatic vascular system and its origin. *Cardiovasc Res* 111: 310 – 321
58. Shafquat A, Joice R, Simmons SL, Huttenhower C (2014) Functional and phylogenetic assembly of microbial communities in the human microbiome. *Trends Microbiol* 22: 261 – 266
59. Baluk P, Yao LC, Flores JC, Choi D, Hong YK, McDonald DM (2017) Rapamycin reversal of VEGF-C-driven lymphatic anomalies in the respiratory tract. *JCI Insight* 2: 90103
60. Tammela T, Zarkada G, Nurmi H, Jakobsson L, Heinolainen K, Tvorogov D, Zheng W, Franco CA, Murtomaki A, Aranda E *et al* (2011) VEGFR-3 controls tip to stalk conversion at vessel fusion sites by reinforcing Notch signalling. *Nat Cell Biol* 13: 1202 – 1213
61. Goldman J, Rutkowski JM, Shields JD, Pasquier MC, Cui Y, Schmokel HG, Willey S, Hicklin DJ, Pytowski B, Swartz MA (2007) Cooperative and

redundant roles of VEGFR-2 and VEGFR-3 signaling in adult lymphangiogenesis. *FASEB J* 21: 1003 – 1012

62. Mortha A, Chudnovskiy A, Hashimoto D, Bogunovic M, Spencer SP, Belkaid Y, Merad M (2014) Microbiota-dependent crosstalk between macrophages and ILC3 promotes intestinal homeostasis. *Science* 343: 1249288
63. Fonseca DM, Hand TW, Han SJ, Gerner MY, Glatman Zaretsky A, Byrd AL, Harrison OJ, Ortiz AM, Quinones M, Trinchieri G *et al* (2015) Microbiota-dependent sequelae of acute infection compromise tissue-specific immunity. *Cell* 163: 354 – 366
64. Amit I, Winter DR, Jung S (2016) The role of the local environment and epigenetics in shaping macrophage identity and their effect on tissue homeostasis. *Nat Immunol* 17: 18 – 25
65. Kim KW, Williams JW, Wang YT, Ivanov S, Gilfillan S, Colonna M, Virgin HW, Gautier EL, Randolph GJ (2016) MHC II+ resident peritoneal and pleural macrophages rely on IRF4 for development from circulating monocytes. *J Exp Med* 213: 1951 – 1959
66. Epelman S, Lavine Kory J, Randolph Gwendalyn J (2014) Origin and functions of tissue macrophages. *Immunity* 41: 21 – 35
67. Sato H, Zhang LS, Martinez K, Chang EB, Yang Q, Wang F, Howles PN, Hokari R, Miura S, Tso P (2016) Antibiotics suppress activation of intestinal mucosal mast cells and reduce dietary lipid absorption in Sprague-Dawley rats. *Gastroenterology* 151: 923 – 932
68. Casley-Smith JR (1962) The identification of chylomicra and lipoproteins in tissue sections and their passage into jejunal lacteals. *J Cell Biol* 15: 259 – 277
69. Sanz E, Yang L, Su T, Morris DR, McKnight GS, Amieux PS (2009) Cell-type-specific isolation of ribosome-associated mRNA from complex tissues. *Proc Natl Acad Sci USA* 106: 13939 – 13944
70. Macpherson AJ, Harris NL (2004) Interactions between commensal intestinal bacteria and the immune system. *Nat Rev Immunol* 4: 478
71. Bernier-Latmani J, Petrova TV (2016) High-resolution 3D analysis of mouse small-intestinal stroma. *Nat Protoc* 11: 1617 – 1629
72. Choi I, Lee S, Kyoung Chung H, Suk Lee Y, Eui Kim K, Choi D, Park EK, Yang D, Ecoiffier T, Monahan J *et al* (2012) 9-cis retinoic acid promotes lymphangiogenesis and enhances lymphatic vessel regeneration: therapeutic implications of 9-cis retinoic acid for secondary lymphedema. *Circulation* 125: 872 – 882
73. Stzepourginski I, Eberl G, Peduto L (2015) An optimized protocol for isolating lymphoid stromal cells from the intestinal lamina propria. *J Immunol Methods* 421: 14 – 19

